Tracer and observationally-derived constraints on diapycnal diffusivities in an ocean state estimate

David S. Trossman[1,2], Caitlin B. Whalen[3], Thomas W. N. Haine[4], Amy F. Waterhouse[5], An T. Nguyen[6], Arash Bigdeli[7], Matthew Mazloff[5], and Patrick Heimbach[6,8]

[1]Department of Oceanography & Coastal Sciences, Louisiana State University, Baton Rouge, USA
[2]Center for Computation & Technology, Louisiana State University, Baton Rouge, USA
[3]Applied Physics Laboratory, University of Washington, Seattle, USA
[4]Department of Earth & Planetary Sciences, Johns Hopkins University, Baltimore, USA
[5]Scripps Institution of Oceanography, University of California, San Diego, USA
[6]Oden Institute for Computational Engineering & Sciences, University of Texas, Austin, USA
[7]EP Analytics, Inc., Austin, USA
[8]Jackson School of Geosciences & Institute for Geophysics, University of Texas, Austin, USA

Correspondence: David S. Trossman (dtrossman@lsu.edu)

Abstract. Use of an ocean parameter and state estimation framework–such as the Estimating the Circulation & Climate of the Ocean (ECCO) framework–could provide an opportunity to learn about the spatial distribution of the diapycnal diffusivity parameter (κ_ρ) that observations alone cannot due to gaps in coverage. However, we show that the assimilation of existing in situ temperature, salinity, and pressure observations is not sufficient to constrain κ_ρ estimated with ECCO, as κ_ρ from ECCO does not agree closely with observations–specifically, κ_ρ inferred from microstructure measurements. We investigate whether there are observations with more global coverage and well-understood measurement uncertainties that can be assimilated by ECCO to improve its representation of κ_ρ. Argo-derived κ_ρ using a strain-based parameterization of finescale hydrographic structure is one potential source of information. Argo-derived κ_ρ agrees well with microstructure. However, because Argo-derived κ_ρ has both measurement and structural uncertainties, we propose dissolved oxygen concentrations as a candidate for future data assimilation with ECCO. We perform sensitivity analyses with ECCO to test whether oxygen concentrations provide information about κ_ρ. We compare two adjoint sensitivity calculations: one that uses misfits to Argo-derived κ_ρ and the other uses misfits to dissolved oxygen concentrations. We show that adjoint sensitivities of dissolved oxygen concentration misfits to the state estimate's control space typically direct κ_ρ to improve relative to the Argo-derived and microstructure-inferred values. However, assimilation of dissolved oxygen concentrations would likely not serve as a substitute for assimilating accurately measured κ_ρ.

1 Introduction

In this paper, we consider the challenges with using observational data products to better inform a data assimilation framework–and, ultimately, better inform us–about the global distribution of ocean mixing. Ocean models must parameterize the unresolved, turbulent diffusion of oceanic tracers because they are unable to resolve the scales of the processes responsible for

20   mixing. Ocean mixing is typically conceptualized in terms of diffusion along and across isopycnal surfaces, and is associated with the transport of isopycnal thickness (or bolus). Ocean models often represent mixing with three parameters: the across-isopycnal mixing parameter (diapycnal diffusivity; *Munk and Wunsch* (1998)), the along-isopycnal mixing parameter (Redi coefficient; *Redi* (1982)), and the eddy isopycnal thickness transport parameter (Gent-McWilliams coefficient; *Gent and McWilliams* (1990)). Diapycnal mixing is an essential component in explaining the observed oceanic stratification (*Munk and

25   Wunsch*, 1998; *Gnanadesikan*, 1999; *Scott and Marotzke*, 2002). Changes in the background diapycnal diffusivity (*Dalan et al.*, 2005; *Krasting et al.*, 2018; *Hieronymus et al.*, 2019; *Sinha et al.*, 2020), Redi coefficient (*Gnanadesikan et al.*, 2015; *Ehlert et al.*, 2017), and Gent-McWilliams coefficient (*Danabasoglu and McWilliams*, 1995) are known to have a profound influence on climate simulations through alterations in the response to surface flux perturbations and changes in ventilation rates. However, the spatiotemporal variabilities found in previous studies of the Redi coefficient (*Abernathey et al.*, 2013; *Bates et al.*, 2014;

30   *Forget et al.*, 2015b; *Cole et al.*, 2015; *Busecke and Abernathey*, 2019; *Groeskamp et al.*, 2020) and Gent-McWilliams coefficient (*Forget et al.*, 2015b; *Katsumata*, 2016; *Bachman et al.*, 2020) fields are virtually absent in ocean models. There is also a dearth of independent observations with which to assess their observationally-derived values (*Cole et al.*, 2015; *Katsumata*, 2016; *Roach et al.*, 2018; *Groeskamp et al.*, 2020), and these values cannot be easily compared with those in models. For instance, it is unclear how to compare Redi coefficients derived from observations with those from models because they are

35   expected to vary with horizontal resolution. Also, the rotational component of eddy transport is not treated the same in many models as in the observationally-derived Gent-McWilliams coefficient product. For these reasons, we focus on the diapycnal diffusivity field–κ_ρ hereafter–in this study.

Parameterizations for κ_ρ (*Gaspar et al.*, 1990; *Large et al.*, 1994) have allowed for a spatiotemporally-varying κ_ρ field, but assessing the performance of these parameterizations has been challenging due to a profound lack of observations. Until

40   recently, the only available observational information about κ_ρ came from tracer release experiments (*Ledwell and Watson*, 1991; *Polzin et al.*, 1997; *Messias et al.*, 2008) and microstructure (i.e., the scales over which molecular viscosity and diffusion are important) measurements of velocity shear (e.g., *Waterhouse et al.* (2014)) or temperature variability (e.g., *Gregg* (1987)). These data are infrequently sampled and cover a relatively small portion of the ocean, but are independent observations with which to compare the more recent global mixing data products. While our understanding of the global distribution of κ_ρ has

45   been transformed by the use of theories to derive κ_ρ from limited observations (*MacKinnon et al.*, 2017; *Whalen et al.*, 2020), none of these observations have been assimilated by existing ocean modeling systems to constrain the κ_ρ field because they are not direct measurements. Currently, the only information about κ_ρ comes from temperature, salinity, and pressure observations in ocean data assimilation systems. If these observations were collected at every location and depth of the ocean, there could be sufficient information to constrain κ_ρ (*Groeskamp et al.*, 2017), but historically, there are spatiotemporal gaps–the reason

50   why we need a data assimilation framework in the first place.

We use the Estimating the Circulation & Climate of the Ocean (ECCO) parameter and state estimation framework to evaluate how near-global, observationally-derived κ_ρ can be used to inform ocean models. The aim of the ECCO framework is to reconstruct the recent history of the ocean (the "state estimate") by filling in the gaps between incomplete observations, which are often sparse and aliased, through data assimilation techniques. The state estimate is much like a reanalysis product (*Heim-

55 *bach et al.*, 2019), but the state estimation framework overcomes some shortcomings by requiring dynamical and kinematical consistency (*Stammer et al.*, 2016). The version 4, release 3 of ECCO (ECCOv4r3; *Fukumori et al.* (2017)) state estimate in our case is achieved by fitting a general circulation model to available observations in a weighted least squares sense (*Wunsch*, 2006; *Forget et al.*, 2015a). The model-data misfit (objective or "cost function") is minimized by varying (i.e., inverting for) a set of uncertain control variables, all of which are independent inputs to the model equations being solved. Importantly for our

60 goal of parameter estimation, the set of control variables may consist not only of initial and boundary conditions, but also of (spatially-varying) model parameters, such as the three used to represent ocean mixing (*Liu et al.*, 2012; *Forget et al.*, 2015a). Since it remains under-explored how well κ_ρ, in particular, is constrained in ECCOv4r3 and how we can provide additional information about κ_ρ, this is the subject of the current study.

To assess whether observations other than temperature, salinity, and pressure can provide useful constraints on the κ_ρ field

65 in ECCOv4r3, we must first perform comparisons of κ_ρ from ECCOv4r3 with κ_ρ from observations, which has not previously been done. We use κ_ρ inferred from microstructure (*Waterhouse et al.*, 2014) and derived from Argo floats (*Whalen et al.*, 2015) to determine whether the ECCO framework needs to improve its κ_ρ using observational constraints (Sections 3.1 and 3.2). It would be possible to assimilate values for κ_ρ derived from theories, which have been shown to agree well with microstructure observations (*Whalen et al.*, 2015). However, because κ_ρ is derived and not measured, an ocean data assimilation system would

70 need to account for both their structural and measurement errors, and their structural uncertainties are not yet well-understood. An alternative approach to constraining κ_ρ is to find a quantity measured with in situ observations (e.g., a transient tracer, as proposed here) that provides information about κ_ρ. Thus, we perform model experiments in forward plus backward ("adjoint") mode to determine whether transient tracer data and observationally-derived κ_ρ provide similar information about how to adjust κ_ρ (Section 3.3). This will help determine whether κ_ρ could be improved by assimilating transient tracer data in a future

75 optimization of an ocean state estimation framework.

2 Methods

2.1 Observationally-derived data products and measured data

2.1.1 Diapycnal Diffusivities

We make use of multiple data sets for κ_ρ derived from observations. (We distinguish between "observations" that are measured

80 quantities using in situ instruments and observationally-derived values, which use measured quantities and a theory to derive values. The former data have only measurement uncertainties, while the latter data have both measurement and structural uncertainties.) These data sets–listed in Table 1–contain values equatorwards of 75^oS and 75^oN, and deeper than about about 250 meters because the method does not yield accurate results in the presence of strong upper-ocean density variability (e.g., *D'Asaro* (2014)).

85 κ_ρ is routinely inferred from the velocity shear measured using microstructure profilers (*Waterhouse et al.*, 2014). We use microstructure-inferred κ_ρ–referred to as $\kappa_{\rho,micro}$ hereafter– (*Osborn*, 1980; *Lueck et al.*, 1997; *Gregg*, 1989; *Moum et al.*,

2002; *Waterhouse et al.*, 2014) to evaluate a model's κ_ρ. (We further distinguish "observationally-inferred" values, which are from the currently accepted method of observing a quantity such as κ_ρ but are not measured, and "observationally-derived" values because the latter data depend on a method that requires additional assumptions.) $\kappa_{\rho,micro}$ are based on an expression for the isotropic turbulence field, which is proportional to the viscosity of water and the velocity shear resolved to dissipative scales (*Thorpe* (2007); and references therein). The depth ranges of the data collected by *Waterhouse et al.* (2014) go from the upper several hundred meters to the full water column. The profiles are seasonally biased at higher latitudes and span decades. There are thousands of vertical profiles that comprise this data set, with samples being taken in North Pacific Ocean, North Atlantic Ocean, tropical Pacific, near Drake Passage, near the Kerguelen Plateau, and in the South Atlantic Ocean. Many of the profiles were taken in regions with both smooth and rough bottom topography. To compare the microstructure profiles with model output, the nearest neighbors to each model's grid are selected, which reduces the data set to 42 profiles.

κ_ρ values are derived from finestructure observations of temperature, salinity, and pressure using a strain-based finescale parameterization, which has been developed and implemented in different ways (*Henyey et al.*, 1986; *Gregg*, 1989; *Polzin et al.*, 1995, 2014), but typically assumes a mixing efficiency of 0.2 (*St. Laurent and Schmitt*, 1999; *Gregg et al.*, 2018). The finescale parameterization assumes that 1) the production of turbulent energy at small scales is due to an energy transfer driven by wave-wave interactions down to a wave breaking scale; 2) nonlinearities in the equation of state, double diffusion, downscale energy transports, and mixing associated with boundary layer physics and hydraulic jumps are neglected; and 3) stationary turbulent energy balance exists where production is matched by dissipation and a buoyancy flux in fixed proportions (*Polzin et al.*, 2014). The implementation by *Whalen et al.* (2015) uses Argo data, assumes a shear-to-strain variance ratio of 3 and a flux Richardson number of $R_f = 0.17$, and determines the fraction of turbulent production that goes into the buoyancy flux (and the rest for dissipation). The finestructure method is not expected to be valid in equatorial regions of the ocean, but nevertheless, the κ_ρ product compares well with microstructure near the equator (*Whalen et al.*, 2015). We use the 2006-2014 climatology of *Whalen et al.* (2015)–referred to as $\kappa_{\rho,W15}$ hereafter–which is a gridded product on an approximately $1^o \times 1^o$ horizontal grid and has three vertical levels: 250-500 meters, 500-1000 meters, and 1000-2000 meters depth. *Whalen et al.* (2015) found that 81% (96%) of their $\kappa_{\rho,W15}$ product is within a factor of 2 (3) of the microstructure measurements. We use this as the basis for the factor of 2-3 uncertainty we cite hereafter.

In addition to the Argo-derived $\kappa_{\rho,W15}$ product, there is ship-based Conductivity, Temperature, and Depth (CTD) hydrography-derived κ_ρ (*Kunze*, 2017)–referred to as $\kappa_{\rho,K17}$ hereafter–that uses the same finestructure parameterization as in the calculation of the $\kappa_{\rho,W15}$ product (see Section 2.2). The vertical resolution of the $\kappa_{\rho,K17}$ product is 256 meters and the horizontal resolution is the spacing between each CTD profile. Data are only included in the $\kappa_{\rho,K17}$ product when the square of the buoyancy frequency is greater than 10^{-7} rad^2 s^{-2} and greater than the square of the Coriolis frequency, $\kappa_{\rho,K17} < 3 \times 10^{-3}$ m^2 s^{-1} is positive, and the depth is deeper than 400 meters.

2.1.2 Dissolved oxygen

In addition to the κ_ρ products, we prepare a tracer for use as a potential constraint on κ_ρ. Dissolved oxygen has vertical gradients that can be resolved by ocean models and has future changes projected to be dependent upon mixing (*Palter and*

Trossman, 2018; *Couespel et al.*, 2019). Oxygen utilization rates within subtropical mode water in the North Atlantic Ocean strongly depend upon vertical mixing (*Billheimer et al.*, 2021). Thus, we choose to include the oxygen climatology from the World Ocean Atlas (2013) in our simulations.

The vertical gradients of these oxygen concentrations, $\partial O_2 / \partial z$, are shown in Fig. 1 for the three depth-averaged bins that

125 *Whalen et al.* (2015) used for their $\kappa_{\rho,W15}$ product. $\partial O_2 / \partial z$ is generally smaller in polar regions, and relatively larger and positive landward of the Gulf Stream, in the Norwegian Sea, off the southern coasts of Mexico and India, near the equator in the Atlantic Ocean, and in the Southern Hemisphere's subtropical gyres of the Pacific and Indian Oceans between 250-500 meters depth (Fig. 1a). The largest positive $\partial O_2 / \partial z$ fill in the gaps between the subpolar regions and the equator at deeper depths (Figs. 1b,c).

130 Co-location of $\partial O_2 / \partial z$ and the dissipation rates calculated by *Whalen et al.* (2015) (see their Fig. 3 compared to Fig. 1 of the present study) suggests there may be information about ocean diapycnal mixing–at least through the *Osborn* (1980) relationship–in oxygen concentrations. The spatial correlation between $\partial O_2 / \partial z$ and the dissipation rates is about -0.2 and increases in magnitude on coarser grids. This indicates a possibly non-local relationship between $\partial O_2 / \partial z$ and dissipation rates. The spatial correlation between $\partial O_2 / \partial z$ and the $\kappa_{\rho,W15}$ is smaller in magnitude–about -0.1. In general, large dissipation rates

135 and κ_ρ values correspond to smaller or more negative $\partial O_2 / \partial z$.

2.2 Modeling system

We use the Estimating the Circulation & Climate of the Ocean (ECCO) framework in our analysis. We use this modeling framework for two purposes: 1) to test whether κ_ρ from ECCO agrees with Argo-derived and microstructure-inferred κ_ρ, given incomplete temperature, salinity, and pressure observations; and 2) to assess whether dissolved oxygen concentrations

140 and observationally-derived κ_ρ provide similar information about how to improve the agreement between κ_ρ from ECCO and observationally-derived data products. ECCO uses a time-invariant but spatially varying κ_ρ field, estimated with an optimization procedure, where κ_ρ associated with temperature and salinity are assumed to be identical. Details about the model simulations we perform are summarized in Table 2.

2.2.1 ECCO

145 The modeling system used here is ECCOv4r3 (*Fukumori et al.*, 2017). The underlying ocean-sea ice model is based on the Massachusetts Institute of Technology general circulation model (MITgcm), which is a global finite volume model. The ECCOv4r3 global configuration uses curvilinear Cartesian coordinates (*Forget et al.* (2015a) - see their Figs. 1-3) at a nominal 1° (0.4^o at equator) resolution and rescaled height coordinates (*Adcroft and Campin*, 2004) with 50 vertical levels and a partial cell representation of bottom topography (*Adcroft et al.*, 1997). The MITgcm uses a dynamic/thermodynamic sea ice compo-

150 nent (*Menemenlis et al.*, 2005; *Losch et al.*, 2010; *Heimbach et al.*, 2010) and a nonlinear free surface with freshwater flux boundary conditions (*Campin et al.*, 2004). The wind speed and wind stress are specified as 6-hourly varying input fields over 24 years (1992-2015). There are 14-day adjustments to the wind stress, wind speed, specific humidity, shortwave downwelling radiation, and surface air temperature. These adjustments are based on estimated prior uncertainties for the chosen atmospheric

reanalysis (*Chaudhuri et al.*, 2013), which is ERA-Interim (*Dee et al.*, 2011). The net heat flux is then computed via a bulk for-
155 mula (*Large and Yeager*, 2009). A parameterization of the effects of geostrophic eddies (*Gent and McWilliams*, 1990) is used.
Mixing along isopycnals is accounted for according to the framework provided by *Redi* (1982). Vertical mixing–diapycnal
plus the vertical component of the along-isopycnal tensor–is determined according to the *Gaspar et al.* (1990) mixed layer
turbulence closure and simple convective adjustment.

Initial conditions and model parameters for the runs performed here are from ECCOv4r3. The least squares problem solved
160 by the ECCO model uses the method of Lagrange multipliers through iterative improvement, which relies upon a quasi-Newton
gradient search (*Nocedal*, 1980; *Gilbert and Lemarechal*, 1989). Algorithmic (or automatic) differentiation tools (*Griewank*,
1992; *Giering and Kaminski*, 1998) have allowed for the practical use of Lagrange multipliers in a time-varying non-linear
inverse problem such as ocean modeling, eliminating the need for discretized adjoint equations to be explicitly hand-coded.
Contributions of observations to the model-data misfit function are weighted by best-available estimated data and model rep-
165 resentation error variance (*Wunsch and Heimbach*, 2007). The observational data assimilated into the ECCO state estimate are
discussed in *Forget et al.* (2015a) and *Fukumori et al.* (2017). These data include satellite-derived ocean bottom pressures, sea
ice concentrations, sea surface temperatures, sea surface salinities, sea surface height anomalies, and mean dynamic topogra-
phy, as well as profiler- and mooring-derived temperatures and salinities (*Fukumori et al.*, 2017). No ocean mixing parameter or
biogeochemical tracer data are assimilated during the ECCO optimization. The control variables that are inverted and optimized
170 for by ECCO include the initial condition of the sea surface heights, ocean velocities, temperatures, and salinities; time-mean
three-dimensional distribution of Redi coefficients (*Redi*, 1982), Gent-McWilliams coefficients (*Gent and McWilliams*, 1990),
and κ_ρ (*Gaspar et al.*, 1990); and time-varying two-dimensional surface forcing fields. Fifty-nine iterations in the optimization
run of ECCO were performed to arrive at the ECCOv4r3 solution we start from for our adjoint sensitivity experiments. The
resulting κ_ρ field in the ECCOv4r3 solution will be referred to as $\kappa_{\rho,ECCO}$ hereafter. While we are presenting some shortcom-
175 ings of the ECCO framework in terms of κ_ρ here, sequential data assimilation systems also have problems with κ_ρ, as shown
in the Appendix.

We run ECCO in two configurations: 1) a "re-run," where all control variables are set to be their estimated values from
ECCOv4r3 in forward mode, and 2) an "adjoint sensitivity" run of the optimized state estimate in forward plus adjoint modes,
where data are included in the cost function but not technically "assimilated" because the model input parameters do not
180 change. An adjoint sensitivity is essentially the sensitivity of one variable to another, computed by making use of the model's
adjoint. Formally, an adjoint sensitivity is $\partial J / \partial X$, where the cost function J is a sum of weighted misfits to observations and a
control variable X is a variable that the model estimates by making use of its adjoint and observations–see Section 2.2.1.1. The
adjoint sensitivities provide information about which directions the model should change X in order to minimize J. (*Masuda
and Osafune*, 2021) showed some examples of adjoint sensitivities of several model parameters in their ocean state estimate to
185 a vertical mixing parameter (slightly different from κ_ρ). We also compute adjoint sensitivities in the present study, but using
ECCO with respect to $X = \kappa_\rho$.

In order to simulate oxygen and phosphate concentrations, several tracers are carried using Biogeochemistry with Light, Iron,
Nutrients and Gases (BLING) model (*Galbraith et al.*, 2015). BLING is an intermediate complexity biogeochemistry model

that uses several prognostic tracers and parameterized, implicit representations of iron, macronutrients, and light limitation and
190 photoadaptation. BLING has been shown to compare well with the Geophysical Fluid Dynamics Laboratory's full-complexity
biogeochemical model, TOPAZ (*Galbraith et al.*, 2015), and has been adapted for use in the MITgcm with its adjoint (*Verdy and Mazloff*, 2017).

The following is a summary of the ECCO experiments we run (Table 2):

- **E-CTRL** - a forward ECCOv4 simulation that uses the parameters from ECCOv4r3; this simulation can be referred to
195   as a "re-run"

- E_κ - an adjoint sensitivity (with respect to $X = \kappa_\rho$) experiment in which only the base-10 logarithm of the $\kappa_{\rho,W15}$ and $\kappa_{\rho,K17}$ products are included in the misfit function J

- E_O - an adjoint sensitivity (with respect to $X = \kappa_\rho$) experiment in which only oxygen concentrations from the World Ocean Atlas (2013) climatology are included in the misfit function J

200 - E_ϵ - an adjoint sensitivity (with respect to $X = \epsilon$) experiment in which only the base-10 logarithm of the $\epsilon_{W15} = \kappa_{\rho,W15}N^2/0.2$ and $\epsilon_{K17} = \kappa_{\rho,K17}N^2/0.2$ products are included in the misfit function J, where the stratification N^2 is from the World Ocean Atlas (2013) climatology

Note that the initial guess for $\kappa_{\rho,ECCO}$ is 10^{-5} m^2 s^{-1} and in the absence of observation-driven adjustments, $\kappa_{\rho,ECCO}$ remains
at or is close to its initial value. Lastly, we analyze the adjoint sensitivities with dissipation rates in the cost function (E_ϵ in
205 Table 2.2) in order to assess whether the stratification–a multiplying factor between κ_ρ and the dissipation rates according to
Osborn (1980)–provides information about κ_ρ.

We take the ECCOv4r3 solution as initial conditions and, with the exception of E-CTRL, we perform an adjoint calculation
for each of the experiments. The adjoint sensitivities are accumulated and averaged over the full integration period. Only one
year was run for each of the adjoint simulations because we are using time-invariant climatologies, and one year suffices to
210 demonstrate the point that the assimilation of a biogeochemical tracer may reduce the bias in κ_ρ. Our results are not qualitatively
sensitive to the run length. The adjoint sensitivities from E_κ are not sensitive to their run length due to the lack of time-
dependence of κ_ρ, but are sensitive to their initial conditions as determined by the ECCOv4r3 solution.

We begin E_O from a previously-derived product that has been spun-up from an initial climatology (*Dutkiewicz et al.*,
2005) because observations do not exist for every grid cell and beginning from this product minimizes model drift. If we
215 were to start from different initial conditions, the model's drift would confound the interpretation of our adjoint sensitivities.
The depth-averaged differences between the uninterpolated World Ocean Atlas (2013) product and the initial conditions for
oxygen concentrations in our ECCO run using BLING are shown in Fig. 2. The differences are largest in the Arctic Ocean,
northeastern Pacific Ocean, and near the coasts, particularly on the eastern side of the American continent, the southwestern
side of the African continent, around the Kuroshio/Sea of Japan region, along almost every coastline of Oceania, and in the
220 Mediterranean Sea (Fig. 2a). These differences are likely due to the deficiencies in model resolution, the sparse observations
in regions such as the Arctic Ocean, the locations of sea ice (*Bigdeli et al.*, 2017), and the parameterization of the tracer air-sea

fluxes (e.g., *Atamanchuk et al.* (2020)). We need to consider the spatial patterns shown in Fig. 2 when interpreting the signs of the adjoint sensitivities.

2.2.2 ECCO adjoint sensitivity analyses

225 In order to understand whether κ_ρ could be estimated more accurately through data assimilation of oxygen concentrations, we need to further explain the details of our adjoint sensitivity experiments with ECCO. We define the objective (or cost) function here to more formally explain what the adjoint sensitivity is. ECCO calculates the cost function to be minimized, J, as (*Stammer et al.*, 2002):

$$J = \sum_{t=1}^{t_f} [\mathbf{y}(t) - \mathbf{S}\tilde{\mathbf{x}}(t)]^T \mathbf{W}(t)[\mathbf{y}(t) - \mathbf{S}\tilde{\mathbf{x}}(t)] \tag{1}$$

230 where t_f is the final time step, $\tilde{\mathbf{x}}$ is the model-based estimate of the state vector $\mathbf{x}$, $\mathbf{S}$ is the observation matrix that relates the model state vector to observed variables (such that $\mathbf{S}\tilde{\mathbf{x}}$ is the model-based estimate of the observables $\mathbf{y}$), and $\mathbf{W}$ is the weight (inverse square of the uncertainty) of the observations. In each of our adjoint sensitivity experiments, the data vector $\mathbf{y}$ only contains the data set specific to the experiment (see Table 2.2) so we emphasize here that J is different for each of our experiments. The uncertainties in $\kappa_{\rho,ECCO}$ in E_κ are set to be three times the values of the observationally-derived κ_ρ because

235 of the level of agreement between the $\kappa_{\rho,W15}$ and $\kappa_{\rho,micro}$ (*Whalen et al.*, 2015). The uncertainties in oxygen concentrations in E_O are set to be 2% of the values of the measured dissolved oxygen concentrations because those are the measurement errors associated with most instruments.

The adjoint sensitivities computed in this study are the derivatives of J in Eq. 1 with respect to κ_ρ. While the adjoint sensitivities of J to the controls space in experiment E_O must be computed online, those in E_κ can either be computed online

240 or offline using an analytical equation (see below). The adjoint sensitivity run with κ_ρ included in the misfit calculation of experiment E_κ can be calculated offline using output from the E-CTRL run instead of being calculated online as follows:

$$\frac{\partial J}{\partial X} = -2\frac{(X_{obs} - X_{model})}{\sigma_X^2}. \tag{2}$$

Here, $X = \kappa_\rho$ is the control variable, $\mathbf{y} = X_{obs}$ is the observationally-derived value of X described in the previous section, $X_{model} = \mathbf{S}\tilde{\mathbf{x}}$ is the value that ECCO estimates for X, and σ_X^2 (entries of $\mathbf{W}$) is taken to be $3X_{obs}$ (or the base-10 logarithm

245 of this in the case of κ_ρ) due to the factor of 2-3 uncertainty. The offline Eq. 2 and online sensitivities have been verified to be in agreement. For X_{model}, we use the offline values calculated from the E-CTRL run following Eq. 2.

Short of assimilating a particular data set (e.g., dissolved oxygen concentrations) in a new optimization run of ECCO, we assess whether the assimilation of a particular data set could lead to a more accurate estimate of a control variable that can be observed (e.g., κ_ρ). Because the observations of κ_ρ here are not direct measurements, we first need to show that observationally-

250 derived κ_ρ has a smaller bias with respect to independent observations than the model's estimate of κ_ρ. We devote the first portion of our study to determining whether $|\kappa_{\rho,W15} - \kappa_{\rho,micro}| < |\kappa_{\rho,ECCO} - \kappa_{\rho,micro}|$ (and, by extension, $\kappa_{\rho,K17}$ in place of $\kappa_{\rho,W15}$) is true. We do this because $\kappa_{\rho,micro}$ is limited in its spatial coverage compared to $\kappa_{\rho,W15}$. However, we don't want to assimilate $\kappa_{\rho,W15}$ (or $\kappa_{\rho,K17}$) because of their observational uncertainties and still limited spatial coverage relative to

dissolved oxygen concentrations. The data product with higher accuracy (dissolved oxygen concentrations) will have larger
255   weights ($\mathbf{W}$ in Eq. 1) and thus will exert more influence in constraining $\kappa_{\rho,ECCO}$–bringing it closer to microstructure values.
So if we can show that the adjustments to κ_ρ in ECCO are similar, whether we provide information from observationally-
derived κ_ρ or a directly measured tracer (dissolved oxygen concentrations), then we would assimilate the tracer. The problem
with doing a direct comparison of the adjustments is that the uncertainties in observationally-derived κ_ρ products are large.
The significance of the correlations between the adjoint sensitivities in E_κ and E_O are difficult to determine with such large
260   uncertainties. Thus, we first quantify the extent to which the adjoint sensitivities from two runs (here, E_κ and E_O) have the
same sign. Specifically, we inspect whether $\partial J/\partial \kappa_\rho$ has the same sign in E_κ and E_O where $|\kappa_{\rho,W15} - \kappa_{\rho,ECCO}|$ is significantly
different from zero (i.e., $\kappa_{\rho,W15}$ is more than a factor of three greater or less than a factor of three smaller than $\kappa_{\rho,ECCO}$).
We perform these comparisons in regions where the difference between the observationally-derived κ_ρ products and $\kappa_{\rho,ECCO}$
exceeds three times the observational products' magnitudes (i.e., statistically distinguishable from zero). In the same regions,
265   we then calculate the correlations between the adjoint sensitivities from E_κ and E_O. Because model errors unrelated to κ_ρ
can confound these correlations, we additionally look at regions where the difference between oxygen concentrations from
the model and the World Ocean Atlas (2013) is relatively small to determine whether oxygen concentrations guide the state
estimate's control space to improve the magnitude of κ_ρ.

3   Results

270   In this study, our first goals are to quantify the biases between κ_ρ from ECCO and κ_ρ from observations. Then we analyze
results from two adjoint sensitivity runs: one with misfits to observed κ_ρ derived from the finescale parameterization and the
other with misfits to observed O_2. We use these results to investigate the potential to use O_2 as a constraint for improving
$\kappa_{\rho,ECCO}$ in a future optimization.

3.1   Model-inverted vs microstructure-inferred κ_ρ comparisons

275   Here, we compare the average $\kappa_{\rho,micro}$ profile that is comprised of 24 campaigns' worth of data (*Waterhouse et al.*, 2014) (see
their Fig. 6; black curve in Fig. 3) with the average $\kappa_{\rho,ECCO}$ profiles and the $\kappa_{\rho,W15}$ product. A geometric average is taken
for each profile because this is more representative than an arithmetic average for a small sample size and when the data are
not normally distributed (*Manikandan*, 2011), like the log-normal distribution of κ_ρ.

    The average κ_ρ profile in the first iteration of ECCO's optimization–i.e., the initial guess of $\kappa_{\rho,ECCO}$–is typically smaller
280   than the microstructure profile, particularly at 1000 m where the difference is approximately an order of magnitude (Fig. 3). At
iteration 59 (which is the ECCOv4r3 solution), the difference between $\kappa_{\rho,ECCO}$ and $\kappa_{\rho,micro}$ decreases. However, agreement
between the average profiles of $\kappa_{\rho,ECCO}$ and $\kappa_{\rho,micro}$ is still worse than the agreement between $\kappa_{\rho,W15}$ and $\kappa_{\rho,micro}$. The
agreement between $\kappa_{rho,W15}$ and $\kappa_{\rho,micro}$ at each of the three depth bins is well within a factor of three (not shown here).

3.2 Model-inverted vs finescale parameterization-derived κ_ρ comparisons

285   We next show $\kappa_{\rho,W15}$ and differences between $\kappa_{\rho,W15}$ and $\kappa_{\rho,ECCO}$ because this highlights the spatial patterns of the adjoint sensitivities in E_κ (see later). The ratio between the $\kappa_{\rho,W15}$ product (Figs. 4a,c,e) and $\kappa_{\rho,ECCO}$ varies throughout the globe (Figs. 4b,d,f). The percent of volume where $\kappa_{\rho,ECCO}$ is at least an order of magnitude different from $\kappa_{\rho,W15}$ is 43.8%. The values of $\kappa_{\rho,ECCO}$ are smaller than those in the observational product in the Kursoshio Extension (500-1000 meters depth), subpolar North Atlantic (500-1000 meters depth), Southern Ocean, equatorial regions in the Atlantic, and shallow (250-500

290   meters depth) Indian and eastern Pacific Oceans (Figs. 4b,d,f). The $\kappa_{\rho,ECCO}$ field is comparatively large in the model's near-equatorial regions, where the intermittency of strong mixing events is likely not captured–even in a time-mean sense–by a time-invariant $\kappa_{\rho,ECCO}$. However, the fidelity of $\kappa_{\rho,W15}$ supplemented with $\kappa_{\rho,K17}$ is unknown near the equator. The fact that $\kappa_{\rho,ECCO}$ and $\kappa_{\rho,W15}$ disagree within the deep mixed layers at high latitudes is not consequential for tracer transport. The errors in $\kappa_{\rho,ECCO}$ could be partially compensating for errors in the vertical component of the along-isopycnal diffusivity

295   tensor and/or numerical diffusion.

The incomplete historical observations of temperature, salinity, and pressure are not sufficient to constrain $\kappa_{\rho,ECCO}$. Values of $\kappa_{\rho,ECCO}$ do not agree well with the observationally-derived κ_ρ ($\kappa_{\rho,micro}$ and $\kappa_{\rho,W15}$), possibly for this reason. While there is an abundance of Argo data in the upper 2000 meters, these data are insufficient to constrain the $\kappa_{\rho,ECCO}$ in a realistic manner. The sparsity of the observations below 2000 meters depth, in high latitude regions, and in some near-coastal areas–

300   where internal wave-induced mixing can be important–is relevant because complete observational coverage of the ocean's temperature, salinity, and pressure could, in principle, better constrain κ_ρ using inverse modeling (*Groeskamp et al.*, 2017). However, the lack of time-dependence of $\kappa_{\rho,ECCO}$, the presence of numerical mixing, and joint estimation of many under-determined parameters in ECCO could also lead to erroneous $\kappa_{\rho,ECCO}$.

3.3 Adjoint sensitivities in ECCO

305   Because the data that get assimilated into ECCO are insufficient to constrain $\kappa_{\rho,ECCO}$ well enough to match $\kappa_{\rho,W15}$ or $\kappa_{\rho,micro}$, assimilating additional variables controlled by mixing may assist in further improving the modeled mixing parameters. Oxygen is a prime candidate since its distribution is, in part, determined by the local κ_ρ. To test this, we run multiple adjoint sensitivity experiments in which either observationally-derived κ_ρ or oxygen is included in the misfit calculation to guide constraints on κ_ρ.

310   We now show the adjoint sensitivity calculations using Eq. 2 for κ_ρ misfits (experiment E_κ in Table 2.2) in Fig. 5; these are later compared with the sensitivities for oxygen concentration misfits in experiment E_O. A positive adjoint sensitivity implies that the misfit can be reduced by decreasing $\kappa_{\rho,ECCO}$. The signs of $\partial J/\partial \kappa_\rho$ (Fig. 5a) are consistent with the signs of disagreement shown in Fig. 4b,e,h, by construction, and with the disagreements with microstructure shown in Fig. 3. Because $\kappa_{\rho,ECCO}$ tends to be very large inside mixed layers, $\partial J/\partial \kappa_\rho$ tends to be positive and larger at many locations in the subpolar

315   latitudes where there are deep mixed layers in the model but possibly not in the real ocean; conversely, $\partial J/\partial \kappa_\rho$ can be negative where the mixed layer depth is too shallow in ECCO, but this isn't the only reason for $\partial J/\partial \kappa_\rho < 0$. The large positive values

of $\partial J/\partial\,\kappa_\rho$ within the mixed layer and some other regions overwhelms the zonal averages in favor of positive values (Fig. 5c). $\kappa_{\rho,ECCO}$ needs to be decreased in many regions at depths shallower than 500 meters to agree better with $\kappa_{\rho,W15}$ and $\kappa_{\rho,K17}$ (red regions in Figs. 4b,d,f), but microstructure measurements (X's in Figs. 4b,d,f) were often taken in locations where

320   $\kappa_{\rho,ECCO}$ should be increased (blue regions in Figs. 4b,d,f) or stay the same. These are regions where there are prominent topographic features and where the centers of subtropical gyres are found.

We next compare $\partial J/\partial\,\kappa_\rho$ from E_κ with $\partial J/\partial\,\kappa_\rho$ from E_O. In E_O, $\partial J/\partial\,\kappa_\rho$ is generally negative in subtropical regions (Figs. 5b,d). Overall, the locations of the positive/negative signs of $\partial J/\partial\,\kappa_\rho$ are not the same everywhere between the E_κ and the E_O experiments, but they agree in many regions (Figs. 5a,c and Figs. 5b,d), which account for nearly two-thirds (three-

325   fourths) of the ocean's volume where they can be compared (in the subtropics, between 20°-50^oN/S, non-white regions in Fig. 6; Table 4). The ocean basin with the highest percent volume of agreement in adjoint sensitivity signs between E_κ and E_O is the subtropical North Atlantic Ocean, with nearly 85% volume agreement. The subtropical South Atlantic Ocean is the only subtropical basin with less than half of its volume in agreement in adjoint sensitivity sign. In general, the tropical regions (between 20^oS and 20^oN) have adjoint sensitivity signs in lesser agreement than the subtropical regions and the subpolar

330   regions (poleward of 50^oN/S) are the regions with the lowest percent volume agreements in adjoint sensitivity signs.

Even with general agreement in signs of sensitivities between E_κ and E_O, we need to address whether this agreement is random–as their correlation is due to the large uncertainties in $\kappa_{\rho,W15}$ and $\kappa_{\rho,K17}$–or underpinned by physical reasons. We first focus on the locations with detectable errors in $\kappa_{\rho,ECCO}$. The regions where the signs of $\partial J/\partial\,\kappa_\rho$ agree from the two experiments (Figs. 6) and have large differences between $\kappa_{\rho,ECCO}$ and the combined $\kappa_{\rho,W15}$ and $\kappa_{\rho,K17}$ product, tend to have

335   relatively small oxygen concentration misfits (Fig. 2). For example, when only regions with less than one standard deviations above the average oxygen concentration misfits are selected, the signs of the adjoint sensitivities agree between E_O and E_κ over 60.8% of the volume with sufficient data. However, the larger the oxygen concentration misfits, the more often the signs of the sensitivities agree. When only regions with more than three standard deviations above the average oxygen concentration misfits are selected, the signs of the sensitivities always agree (yellow regions in Fig. 6). Given the good agreement in signs of

340   the sensitivities in regions with large κ_ρ misfits, we next inspect the sensitivity sign patterns in regions with small κ_ρ misfits.

The vast majority of the locations where disagreements occur in sensitivity signs are in places with statistically indistinguishable differences between $\kappa_{\rho,ECCO}$ and $\kappa_{\rho,W15}$ supplemented with $\kappa_{\rho,K17}$ (white regions in Fig. 6 that are non-white in Fig. 5). The regions with statistically indistinguishable differences in κ_ρ account for 56.2% of the volume of the ocean where the adjoint sensitivities from E_O and E_κ can be compared. Within these regions, there are differences in the signs of the

345   sensitivities in locations where κ_ρ is not expected to dominate the variability in oxygen. These regions include, for example, the equatorial Pacific and Atlantic Oceans, where *Palter and Trossman* (2018) and *Brandt et al.* (2021) point out that ocean circulation changes significantly influence long-term changes in oxygen. Another example is in the open subpolar North Atlantic Ocean (the blue region in the Labrador Sea in Fig. 6a), where *Atamanchuk et al.* (2020) present observational evidence that air-sea fluxes mediated by bubble injection–not represented by ECCO–dominate the variability in oxygen down to 1000

350   meters depth. When these tropical and subpolar regions (outside of the $20^o - 50^o$N/S bands) are excluded, the percent volume of the ocean where the signs of the adjoint sensitivities agree between E_κ and E_O increases. Given that there are known phys-

ical processes not dominated by κ_ρ causing variations in oxygen concentrations in regions outside of the (sub)tropics where there are statistically insignificant differences between $\kappa_{\rho,ECCO}$ and the observationally-derived κ_ρ, our interpretation of the patterns shown in Figs. 5 and 6 is that κ_ρ controls much of the variability in oxygen concentrations in the (sub)tropical regions.

355 This is one indication that dissolved oxygen concentrations could provide information about κ_ρ.

We further address whether the potential information dissolved oxygen concentrations provide about κ_ρ is due to the information oxygen contains about stratification. We do this by using the adjoint sensitivity results obtained from experiment E_ϵ with observationally-derived dissipation rates, $\epsilon = N^2 \kappa_\rho / 0.2$–where N^2 is the stratification–instead of κ_ρ, in the misfit function via Eq (2) and multiply the adjoint sensitivity of E_O by $0.2/N^2$ so that their sensitivities are each taken with respect

360 to ϵ (parentheses in Table 4). We find approximately equal agreement between the signs of the adjoint sensitivities from E_O (scaled by $0.2/N^2$) and E_ϵ as we do between those from E_O and E_κ in every region. Because ϵ is related to κ_ρ through the stratification, we suggest that the information oxygen concentrations provide about κ_ρ is likely independent of the stratification field.

Lastly, in order to examine whether there is a statistically significant relationship between the adjoint sensitivities from E_κ

365 and E_O. We again focus on the regions where the difference between $\kappa_{\rho,ECCO}$ and observational κ_ρ products (from Argo and microstructure) is statistically significant (greater than a factor of three), but also filter out the adjoint sensitivities where the differences between oxygen concentrations from ECCO and those from the World Ocean Atlas (2013) are statistically significant. The correlations tend to be small but positive (Fig. 7). However, if we perform Monte Carlo simulations where we sample κ_ρ values within its uncertainty and recompute the adjoint sensitivity for E_κ and then its correlation with that for

370 E_O, the maximum correlatons we find are larger, particularly where the adjoint sensitivities are both negative (Figs. 7a,c). This suggests that $\kappa_{\rho,ECCO}$ may be at least partially constrained by the information provided by oxygen concentrations. That is, oxygen concentrations inform adjoint sensitivities that typically direct $\kappa_{\rho,ECCO}$ to improve relative to observationally-derived κ_ρ. Constraints that the assimilation of oxygen concentrations may have on $\kappa_{\rho,ECCO}$ may be beneficial, but not a perfect substitute for the assimilation of accurately measured κ_ρ itself.

375   4   Discussion and Concluding Remarks

4.1   Discussion

This study evaluated the potential to improve the diapycnal diffusivities (κ_ρ) in the ECCOv4 ocean parameter and state estimation framework. We assessed the fidelity of the inverted field of $\kappa_{\rho,ECCO}$ by first comparing the average observed vertical profiles of $\kappa_{\rho,ECCO}$ with those inferred from microstructure. The comparison was not favorable. $\kappa_{\rho,ECCO}$ is inverted for

380 within the ECCO framework through constraints of vertical profiles of temperature and salinity–e.g., from Argo profiles. The low fidelity suggests that these hydrographic data alone are not sufficient to constrain $\kappa_{\rho,ECCO}$, but there may be some model errors that would lead to errors in $\kappa_{\rho,ECCO}$ even in the presence of globally complete hydrographic observations (see Section 4.2).

We then investigated which additional observations can be used as new constraints to improve the fidelity of the inverted
$\kappa_{\rho,ECCO}$. The products we used were observationally-derived κ_ρ based on Argo (the W15 product) and ship-based CTD (the
K17 product) hydrographic data and oxygen concentration (*WOA*, 2013). To justify the use of the observationally-derived κ_ρ
products, we also evaluated them by comparing them with the microstructure-inferred product. $\kappa_{\rho,W15}$ and $\kappa_{\rho,W17}$ have better
agreement with the microstructure-inferred data than $\kappa_{\rho,ECCO}$ does.

We inspected the misfit of the model parameter $\kappa_{\rho,ECCO}$ with respect to $\kappa_{\rho,W15}$ and $\kappa_{\rho,K17}$ and motivated use of dissolved
oxygen concentration data as a potential constraint in ECCO. One drawback of the observationally-derived data products
for κ_ρ is that they have large uncertainties (here, approximated by a factor of three). Observed oxygen concentrations, on
the other hand, has smaller relatively uncertainty. More importantly, we showed that vertical oxygen gradients have similar
geographical patterns to energy dissipation rates. We therefore performed an additional adjoint sensitivity experiment with
oxygen concentration data as the only data in the misfit function. Adjoint sensitivities results were compared between the
experiment with measured oxygen in the misfit function and observationally-derived κ_ρ in the misfit function. Regions where
the sensitivities agree in signs between the two experiments are locations where we believve adjustments in κ_ρ, as informed by
these data, can help improve $\kappa_{\rho,ECCO}$. These regions include nearly three-quarters of the volume of comparable seawater in the
subtropics. Correlations between adjoint sensitivities from each experiment are positive where differences between the oxygen
concentrations in the model and observations are relatively small. These findings suggest that dissolved oxygen concentrations
could be used to more accurately estimate κ_ρ in a newly optimized ECCO solution. However, given the magnitudes of the
correlations between the adjoint sensitivities, assimilation of observationally-derived κ_ρ could (additionally) be necessary,
especially if their uncertainties are better quantified.

4.2 Caveats and future directions

Many factors–including a significant absence of independent observations for assessment, a combination of measurement and
structural errors, numerical diffusion in our simulations, and unconstrained parameters in the biogeochemical modules–have
stymied progress in state estimation of ocean mixing parameters. First, only one ocean mixing parameter–namely, κ_ρ–has been
compared with independent observational data–specifically, microstructure. This is the primary reason why we focused on κ_ρ
in our study. Second, the ECCO-estimated κ_ρ accounts for other model errors (e.g., structural ones suggested by *Polzin et al.*
(2014)), which explains some of the model biases relative to microstructure observations. For instance, the ECCO-estimated κ_ρ
should be time-dependent as well as spatially-varying, but it is only spatially-varying. In the presence of other estimated model
parameters and initial conditions, some parameters could be compensating for errors in κ_ρ. Additionally, there is numerical
diffusion in the model, which could confound some physical inferences about the model (e.g., regarding how sensitive the
model's state is to κ_ρ relative to along-isopycnal diffusion). Numerical errors could remain and result in the primary source
of error in the ocean state estimate if sufficient constraints are placed on κ_ρ in ECCO. Lastly, there are several unconstrained
parameters in biogeochemical modules used to calculate biogeochemical tracers (*Verdy and Mazloff*, 2017), so some of the
disagreements in signs of the adjoint sensitivities found here could be associated with other inaccurate parameters.

These challenges can continue to be overcome by allowing models and observations to inform each other. First, the observationally-derived κ_ρ from the finescale parameterization could be further scrutinized using ship-based CTD data taken concurrently with microstructure velocity shear data. A preliminary analysis suggests that the percent difference between the full depth-averaged

420 microstructure CTD-derived κ_ρ from the finescale parameterization and the microstructure-inferred κ_ρ is indistinguishable from zero (1.68%), but the quality of the the microstructure CTD data has not been fully assessed. Second, we would need to account for the time-dependence of κ_ρ in a future ocean state estimate. The under-determined nature of the parameter estimation procedure makes this difficult. These efforts would also benefit from minimizing spurious mixing due to numerical diffusion (e.g., *Holmes et al.* (2021)) through choosing a different advection scheme, but this would add computational expense.

425 The effective proxy potential framework of *Loose and Heimbach* (2021) could be used to indicate whether measurements of oxygen concentrations in particular locations are more informative of κ_ρ than in other locations. We did not pursue this in the present study because our adjoint runs use a global misfit; if we perform an ensemble of adjoint sensitivity runs with a single observation in each run, then we could calculate the effective proxy potential at each of these observation locations. Third, unconstrained parameters in the biogeochemical modules could potentially be circumvented. One potential way to do this is

430 by assimilating preformed oxygen (i.e., oxygen without any biological influence, making it a passive tracer) instead of oxygen concentrations. Observationally-derived transit-time distributions with a maximum entropy-based method from previous studies (e.g., *Khatiwala et al.* (2009); *Zanna et al.* (2019)) or from a tracer-informed ocean state estimate (*DeVries and Holzer*, 2019) can help derive preformed oxygen from oxygen concentration observations. Lastly, the (imperfectly-known) initial conditions of each biogeochemical tracer will also need to be included in the input control vector during optimization of the ocean

435 state estimate. Our results suggest that the assimilation of biogeochemical tracers will help build a more complete representation and understanding of κ_ρ, and the next step is to perform another optimization of the ocean state estimate including these tracer observations.

Appendix A: Model with a sequential data assimilation framework

A1 GEOS-5 and the GMAO S2S Ocean Analysis

440 To demonstrate a problem with κ_ρ in a sequential data assimilation framework, we present example output from a reanalysis product and output from an identical ocean model hindcast without any data assimilation. GEOS-5 includes a global, finite volume atmospheric general circulation model that is used for numerical weather prediction, seasonal-to-decadal forecasts, and as the background field for atmospheric reanalyses (*Molod et al.*, 2015). The ocean is represented by the GFDL Modular Ocean Model (*Griffies et al.*, 2015), version 5 (MOM5) and the Los Alamos Community Ice CodE sea ice model (*Hunke et al.*,

445 2013), version 4.1 (CICE4.1). We use a configuration of the GEOS-5 modeling system with a 1° (0.5^o at equator) resolution on a tripolar (*Murray*, 1996) staggered Arakawa B-grid (*Mesinger and Arakawa*, 1976) and 50 geopotential levels for MOM5, 2° resolution and 24 pressure levels for the atmospheric model, and 1° resolution and 3 layers for CICE4.1. Historical aerosols (sulfate, dust, and sea salt) and biomass burning emissions (black and organic carbon) updated from the Goddard Chemistry Aerosol Radiation and Transport (GOCART) model (*Chin et al.*, 2002) are used over the time period 1992 through 2016. Initial

450 conditions are based on a long spin-up that used MOM4 coupled to one version of the GEOS-5 atmosphere model (*Molod et al.*, 2012) and hundreds of additional years of spin-up that used MOM4 coupled to a slightly different version of the GEOS-5 atmosphere model. The differences between the two versions of the GEOS-5 atmospheric model used in the two phases of spin-up include developments in cloud microphysics and atmospheric chemistry.

κ_ρ, Redi coefficients, and Gent-McWilliams coefficients are determined in MOM5 as follows. κ_ρ in MOM5–$\kappa_{\rho,GEOS5}$

455 hereafter–is represented by the K-Profile Parameterization (KPP; *Large et al.*, 1994) and a parameterization for mixing due to internal tides (*Simmons et al.*, 2004). Shear-driven mixing, gravitational instabilities that can cause vertical convection, and double-diffusive processes, which can cause the temperature diffusivity to be different from the salinity diffusivity, are accounted for in the interior (*Large et al.*, 1994). The resulting $\kappa_{\rho,GEOS5}$ field spatio-temporally varies. However, this combination of parameterizations does not make use of an explicit energy budget that accounts for conversion between kinetic and

460 potential energy when determining $\kappa_{\rho,GEOS5}$. The Redi coefficients (*Redi*, 1982) and Gent-McWilliams coefficients of the (*Gent and McWilliams*, 1990) parameterization for mesoscale eddies are, by default, prescribed to be 600 m^2 s^{-1} everywhere, except for some variation in western boundary current regions for the Gent-McWilliams coefficients. The Redi coefficients and Gent-McWilliams coefficients are, thus, constant in time and in most locations. A mixed layer instability scheme for the submesoscale transport by (*Fox-Kemper et al.*, 2011) is used.

465 We use a reanalysis product, which uses the same underlying modeling system as the GEOS-5 coupled earth system model, called the Global Modeling and Assimilation Office sub-seasonal to seasonal (GMAO S2S) Ocean Analysis. The output of the GMAO S2S Ocean Analysis highlights how κ_ρ can behave due to the disruption of dynamical balance that can be the result of the use of a sequential data assimilation system (*Stammer et al.*, 2016; *Pilo et al.*, 2018). The GMAO S2S Ocean Analysis only assimilates hydrographic information to constrain κ_ρ and relies on the same parameterizations as GEOS-5's ocean component

470 to calculate κ_ρ.

The NASA GMAO has recently updated their GEOS-5 sub-seasonal to seasonal forecast system (S2S-v2.1; https://gmao.gsfc.nasa.gov/cgi-bin/products/climateforecasts/geos5/S2S_2/index.cgi). This new system is the current contribution of the GMAO to the North American Multi-Model project (http://www.cpc.ncep.noaa.gov/products/NMME/about.html) and NOAA's experimental sub-seasonal ensemble project

475 (http://cola.gmu.edu/kpegion/subx/index.html). A configuration of the modeling system is used that is nominally 0.5^o resolution on a tripolar (*Murray*, 1996) staggered Arakawa B-grid (*Mesinger and Arakawa*, 1976) and 40 geopotential levels for MOM5, and 0.5^o resolution and 5 layers for CICE4.1 with atmospheric forcing from MERRA-2 (Modern-Era Retrospective analysis for Research and Applications, Version 2) reanalysis (*Gelaro et al.*, 2017). The GMAO S2S Ocean Analysis (*Molod et al.*, 2020) is a reanalysis product that uses a system similar to the Local Ensemble Transform Kalman Filter (LETKF) data

480 assimilation procedure described by (*Penny et al.*, 2013), but where the background error is calculated offline using ensemble members of freely coupled simulations. The background error does not explicitly account for uncertainties in the ocean mixing parameters, as it is only a function of the observed and background temperatures and salinities. The temperature and salinity would change and so would the calculated covariances if the mixing parameterizations were changed, but each of the 21 background free-running simulations have the same mixing parameterization, as they only differ in their initialization.

485 The following datasets were used by the GMAO S2S data assimilation modeling system. A relaxation procedure, or update, is applied towards the MERRA-2 sea surface temperatures and sea ice fraction from the NASA TEAM-2 product (*Markus et al.*, 2009) at a 5-day assimilation cycle. No ocean mixing parameter data are assimilated. Assimilated in situ observational data that provide temperatures and salinities come from TAO, PIRATA, RAMA, XBT, CTD, and Argo instruments. Satellite altimetry data that provide sea level anomalies come from TOPEX, ERS-1+2, Geosat FO, Jason-1, Jason-2, Jason-3, Envisat,

490 Cryosat-2, Saral, HY-2A, and Sentinel 3A. The absolute dynamic topography is calculated as the sum of the sea level anomaly and the mean dynamic topography, which is estimated using GOCE and GRACE data, all available altimetry, and in situ data. Absolute dynamic topography data are assimilated into the model system using the same method as for the in situ data, except these data are thinned along-track and a Gaussian weighted mean using a decorrelation scale of 1000 km is calculated prior to assimilation. In addition, the global trend was removed from the absolute dynamic topography before assimilation and

495 zero net input of water was applied. Precipitation is corrected using the Global Precipitation Climatology Project version 2.1 (GPCPv2.1, provided by the NASA/Goddard Space Flight Center's Laboratory for Atmospheres, which calculates the dataset as a contribution to the GEWEX Global Precipitation Climatology Project) and Climate Prediction Center (CPC) Merged Analysis of Precipitation (CMAP, provided by the NOAA/OAR/ESRL PSD, Boulder, Colorado, USA, from their website at http://www.esrl.noaa.gov/psd/), as described by (*Reichle et al.*, 2011) except for MERRA-2 instead of MERRA data. All other

500 atmospheric forcing fields used in the construction of the reanalysis came from MERRA-2. The GMAO S2S modeling system is an update to the one described in (*Borovikov et al.*, 2017). As such, the model only ran for the period: May of 2012 to March of 2019.

A2 Steric sea level budget framework

In order to examine whether the analysis increments can dynamically impact κ_ρ, we analyze a model's buoyancy budget, which
505 is broken down into heat and salt budgets and used to calculate the steric sea level budget. The tracer tendency equation terms
required for the heat and salt budgets were computed online and saved as the reanalysis was running. The tracer equations can
be broken down into individual contributions (*Palter et al.*, 2014),

$$\rho\frac{d\Theta}{dt} + \rho A^\Theta = -\nabla \cdot \mathbf{J}^\Theta + \rho Q^\Theta \qquad\qquad (A1)$$
$$\rho\frac{dS}{dt} + \rho A^S = -\nabla \cdot \mathbf{J}^S + \rho Q^S,$$

510 where $d/dt = \partial/\partial t + (\mathbf{v} + \mathbf{v}^*) \cdot \nabla$ is the material derivative, $\mathbf{v}$ is the resolved velocity field, $\mathbf{v}^*$ is the eddy-induced or quasi-
Stokes velocity field that represents parameterized motions, Θ is the potential temperature, S is the salinity, ρ is the locally
referenced potential density, $\mathbf{J}^\Theta$ and $\mathbf{J}^S$ are the parameterized along-isopycnal and diapycnal mixing fluxes associated with
potential temperature and salinity, Q^Θ and Q^S are the sums of sources and sinks of potential temperature and salinity, and
A^Θ and A^S are the analysis increments for potential temperature and salinity due to the assimilation of data by a sequential
515 filter-based data assimilation ocean modeling system. The analysis increments in a sequential filter-based data assimilation
system can obscure the physics.

The heat and salt budget terms summarized by Equation (A1) are computed as follows. The resolved, mesoscale, and
submesoscale transports are accounted for in the material derivatives Θ and S, the neutral and diapycnal diffusion of Θ and
S are accounted for by $\mathbf{J}^\Theta$ and $\mathbf{J}^S$, and the analysis increments of Θ and S are accounted for by A^Θ and A^S. The neutral
520 diffusion term includes cabbeling, thermobaricity, and a dianeutral contribution that mixes properties by providing for the
exponential transition to horizontal diffusion in regions of steep isoneutral slopes according to (*Treguier*, 1992) and (*Ferrari
et al.*, 2008, 2010) where the surface boundary layer is encountered and following (*Gerdes et al.*, 1990) next to solid walls.
The diapycnal diffusion term is not added to the vertical component of the along-isopycnal diffusion term, but because of
convention (e.g., *Palter et al.*, 2014) is nevertheless referred to as the vertical diffusion term hereafter. The vertical diffusion
525 term also includes penetrating shortwave radiation flux. The sources and sinks of Θ and S accounted for by Q^Θ and Q^S include
nonlocal convection (the transport where turbulent fluxes don't depend upon local gradients in Θ or S because buoyant water
gets entrained into the mixed layer when the surface buoyancy forcing drives convection above a stratified water column);
surface buoyancy fluxes (latent, sensible, shortwave, longwave, and frazil heat fluxes); precipitation minus evaporation; runoff
mixing (mixes properties associated with river outflows); downslope mixing (mixes properties downslope to represent the
530 overflow dense waters from marginal seas); sigma-diffusion (mixing properties along terrain-following coordinates in regions
with partial bottom cells); numerical smoothing of the free surface (intended to reduce B-grid checkerboard noise); numerical
sponge (intended to absorb the Kelvin waves set off by the assimilation of some data); calving of land ice; and frazil ice
formation. The runoff mixing, downslope mixing, and sigma-diffusion terms are considered sources or sinks here because they
are associated with numerical schemes that aim to resolve problems created by coarse model resolution, the vertical coordinate
535 system used near boundary layers, and imperfect bathymetry. There is no geothermal heating included in the GMAO S2S

Ocean Analysis. The vertical diffusion term includes a subsurface shortwave heating contribution to a function of the κ_ρ field, the mesoscale transport term assumes constant Gent-McWilliams coefficients, and the neutral diffusion term assumes constant Redi coefficients.

At each time step, the model evaluates a tendency term for every process that contributes to (A1) from their parameterized

540   or dynamically calculated values, their units are converted to W m^{-2} and kg m^{-2} s^{-1} for Θ and S, and their monthly averages are saved to the output files used in this analysis. Implicit in these output tendency terms is that each term is weighted by the thicknesses of each layer as the model runs and writes the output to file. The heat and salt budget terms saved to file are used to calculate the steric sea level budget as follows. The steric sea level budget terms are computed by scaling the heat tendency terms by α/C_p and the salt tendency terms by -1000β, where C_p (units in J kg^{-1} K^{-1}) is the specific heat of seawater,

545   $\alpha = -[1/\rho](\partial\rho/\partial T)$ (units in K^{-1}) is the thermal expansion coefficient, and $\beta = [1/\rho](\partial\rho/\partial S)$ (units in kg g^{-1}) is the haline contraction coefficient. In order to get a longitude-latitude map of the terms that depend upon depth shown here, we integrate over depth by summing over the depth dimension. We analyze part of the steric sea level budget of the GMAO S2S Ocean Analysis to examine the relationships between different terms.

Appendix B: Results for the sequential data assimilation framework

550   ### B1   Assessments of κ_ρ from models

First, we compare the average $\kappa_{\rho,micro}$ profile that is comprised of 24 campaigns worth of data (*Waterhouse et al.*, 2014) (see their Fig. 6; black curve in Fig. A1a) with the average model-calculated κ_ρ profiles and $\kappa_{\rho,W15}$. A geometric average is taken for each profile because a geometric average is more representative than an arithmetic average for a small sample size and when the data are not normally distributed (*Manikandan*, 2011), like the log-normal distribution of κ_ρ.

555   We compare microstructure (black curve in Fig. A1a) with GEOS-5 (red curve in Fig. A1a). $\kappa_{\rho,GEOS5}$, on average, is in close agreement with microstructure over the upper 250-2000 meters. On average, the disagreement with microstructure and Argo is approximately the same as the disagreement between microstructure and GEOS-5. All three κ_ρ are well within the uncertainty of the Argo product. The profiles are also within the temporal variability in $\kappa_{\rho,GEOS5}$ below the mixed layer depths (Fig. A1b; also see Fig. 9 in (*Whalen et al.*, 2015)). The temporal variability in κ_ρ is only large near regions with

560   active deep convection (e.g., between 40-50°N in the North Atlantic, as shown in Fig. A1b). The blue and green diamonds in Fig. 1c of (*Waterhouse et al.*, 2014) show that there are only a few microstructure profiles are within the 40-50°N band in the North Atlantic. These are all near the east coast of North America, not in regions that experience deep convection so the temporal variability in microstructure is not expected to be large enough that the disagreements in κ_ρ can be explain by temporal sampling/aliasing.

565   While the average $\kappa_{\rho,GEOS5}$ profile is fairly accurate, particularly below 500 meters depth (red curve in Fig. A1), $\kappa_{\rho,GMAO}$ is in much worse agreement with microstructure (green curves in Fig. A1). The large values of $\kappa_{\rho,GMAO}$ are not due to a few isolated locations. $\kappa_{\rho,GMAO}$ is too large below about 250 meters depth (solid green curve in Fig. A1). The average profile of $\kappa_{\rho,GMAO}$ is generally constant or decreases with depth, as opposed to the average profiles of $\kappa_{\rho,GEOS5}$ and microstructure,

which generally increase with depth. Potential reasons for the large disagreements between $\kappa_{\rho,GMAO}$ and microstructure

570 include dynamical adjustments due to the GMAO S2S Ocean Analysis' analysis increments, inconsistencies between the model's atmosphere and ocean due to the strong relaxation to sea surface temperatures, fixed zero net water input for global sea level, and numerics such as the techniques applied to damp the waves created from assimilating some observations.

B2   Model- vs finescale parameterization-derived κ_ρ comparisons

While comparisons with microstructure reveal general agreement with the average profile of $\kappa_{\rho,GEOS5}$–except near the surface

575 and at deep depths–we also want to assess whether there are deficiencies in the average geographic distribution of $\kappa_{\rho,GEOS5}$ by comparing the output of GEOS-5 with the $\kappa_{\rho,W15}$ product. Comparing the $\kappa_{\rho,GEOS5}$ field with the $\kappa_{\rho,W15}$ results in better agreement than the similar comparisons between $\kappa_{\rho,GMAO}$ and $\kappa_{\rho,W15}$. For example, $\kappa_{\rho,GEOS5}$ only disagrees with $\kappa_{\rho,W15}$ by more than a factor of 3 over 36.6% of grid points with available data (Fig. A2b), while the disagreement doubles in percentage (79.1%) for $\kappa_{\rho,GMAO}$ (Fig. A2a). The errors in $\kappa_{\rho,GEOS5}$ are smaller than $\kappa_{\rho,GMAO}$. Thus, when the objective

580 of the GMAO S2S Ocean Analysis is to minimize the misfit between the model and observations of temperature, salinity, and some surface characteristics, κ_ρ can be better represented without any observational constraints; i.e., the GMAO S2S Ocean Analysis improves temperature and salinity misfits for the wrong reasons.

The regions with the largest disagreement between $\kappa_{\rho,GEOS5}$ and $\kappa_{\rho,W15}$ are along the equator, in the Southern Ocean, in the Labrador and Irminger Seas, and in the Gulf Stream and Kuroshio Extensions (Fig. A2b). Along the equator the values

585 of $\kappa_{\rho,GEOS5}$ tend to be larger than the observational product, but the discrepancy changes sign slightly poleward in the near-equator tropics. Inadequate resolution and parameterization of diapycnal mixing can cause too little mixing to occur in these regions as well as in the Southern Ocean and along mid-ocean ridges (*MacKinnon et al.*, 2017). The values of $\kappa_{\rho,GEOS5}$ are smaller than the observations both in regions where deep convection is prevalent and in the vicinity of the Antarctic Circumpolar Current (ACC). In the Gulf Stream Extension region, the Malvinas Current region, part of the Kuroshio Extension region, and

590 the Indian Ocean sector of the ACC above 500 meters depth, the values of $\kappa_{\rho,GEOS5}$ are too large. This is because $\kappa_{\rho,GEOS5}$ can be much increased inside the mixed layer depth, which can be deeper than 250 meters due to vertical convection. One possible source of these errors in the abyssal κ_ρ is the improper treatment of remote internal tide-induced mixing, discussed in (*Melet et al.*, 2016), but several other processes can impact κ_ρ in the upper water column. For example, the wind-driven near-inertial waves (*Alford et al.*, 2016) can be important near the surface in many locations, and internal tide breaking is

595 important near the seafloor at low latitudes in the Northern Hemisphere (*Arbic et al.*, 2004; *Nycander*, 2005; *Melet et al.*, 2013; *MacKinnon et al.*, 2017) and beneath the ACC, where lee wave breaking is important (*Nikurashin and Ferrari*, 2011; *Scott et al.*, 2011; *Naveira Garabato et al.*, 2013; *Melet et al.*, 2014; *Wright et al.*, 2014; *Trossman et al.*, 2013, 2016; *Yang et al.*, 2018). (*MacKinnon et al.*, 2017) discusses other candidates for more accurate representation of κ_ρ. Identifying the sources of errors in $\kappa_{\rho,GEOS5}$, particularly in the abyss, is beyond the scope of the present study. We emphasize the much greater errors

600 in $\kappa_{\rho,GMAO}$ and next examine whether the analysis increments could be one source of these larger errors (either directly or by way of altering the velocity field).

B3   Relationships between steric sea level budget terms

We now examine whether the velocity field itself changes because of the analysis increments. To do this, we show the relationship between the analysis increments and resolved advection terms in the steric sea level budget for the GMAO S2S Ocean
605   Analysis in Fig. A3a. The Pearson correlation coefficient between the analysis increments and resolved advection terms in the steric sea level budget is about -0.3. The magnitudes of the analysis increments are determined by the temperature, salinity, and sea surface height fields, and the analysis increments and the resolved advection term in the GMAO S2S Ocean Analysis are comparable in size for both heat and salt tendencies–the largest terms in each budget in their zonal averages at most latitudes. However, previous studies have shown that analysis increments induce changes in the velocity field via dynamic adjustment
610   (*Stammer et al.*, 2016; *Pilo et al.*, 2018). The correlation between the analysis increments and resolved advection terms shown in Fig. A3a are consistent with the findings of these previous studies. The role of the analysis increments, by a similar argument, could be extended to the introduction of physically inconsistent air-sea exchanges; we next show that these factors at least partially cause errors in $\kappa_{\rho,GMAO}$. There are distortions in temperature and salinity fields from applying analysis increments, violating conservation principles and potentially causing the model to undergo baroclinic adjustment (Stammer et al.,
615   2016). The Pearson correlation coefficients between the diapycnal diffusion terms and the analysis increment terms in the heat and salt budgets over all locations are about 0.7 (Fig. A3b), suggesting that the analysis increments are associated with errors in $\kappa_{\rho,GMAO}$. Problems with the physical consistency of air-sea exchanges–due to relaxation of sea surface temperatures and requiring net zero water input–could also contribute to the errors in $\kappa_{\rho,GMAO}$. The correlation between the surface flux and diapycnal diffusion terms in the heat and salt tendency budgets are fairly well correlated–Pearson correlation coefficient of
620   about -0.4 (Fig. A3c), suggesting that there is an association between the surface flux errors and errors in $\kappa_{\rho,GMAO}$. Given these correlations and the way analysis increments and physical inconsistencies of air-sea exchanges are implemented in the GMAO S2S Ocean Analysis, errors in $\kappa_{\rho,GMAO}$ must be caused by analysis increments (and possibly adjustments of air-sea exchanges) rather than the other way around.
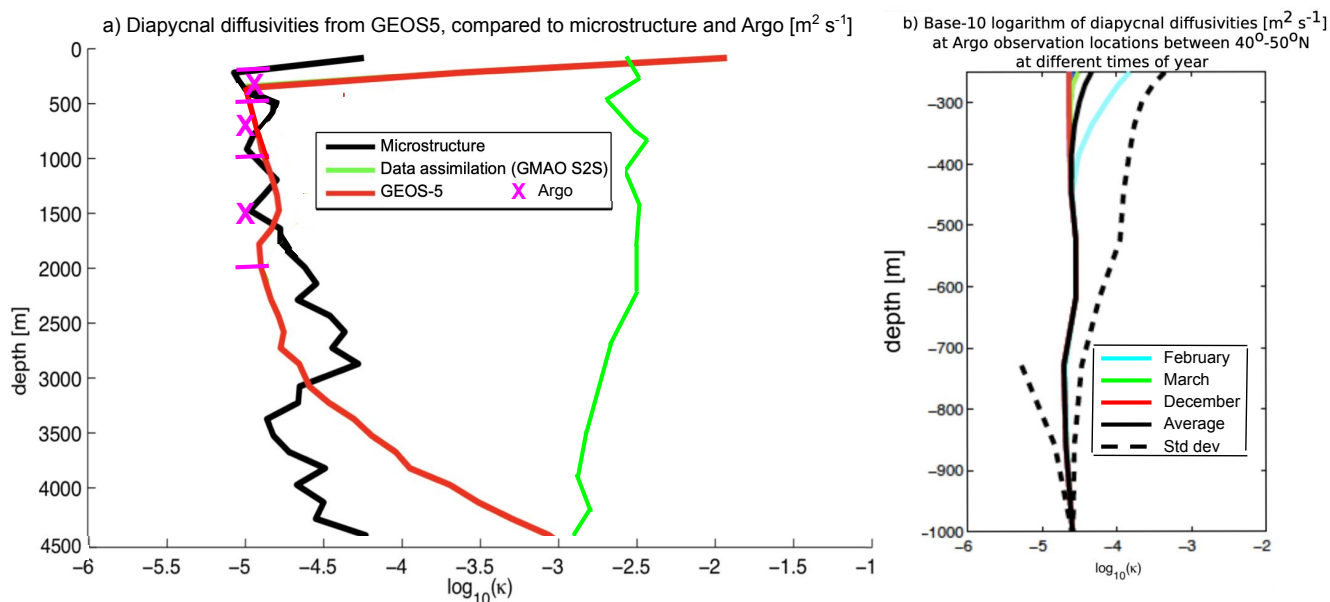
Figure A1. κ_ρ profiles (panel a) averaged over all microstructure observation locations from the 24-year-average of the free-running GEOS-5 simulation (G-CTRL - red curve). Also shown is the average of κ_ρ profiles from the 24 full-depth microstructure observations (black curve) presented in (*Waterhouse et al.*, 2014) (see their Fig. 6) and the average of κ_ρ (magenta X's bounded by horizontal lines) at each of the depth bins in the (*Whalen et al.*, 2015) product. At each location, the simulated profiles are extracted and the base-10 logarithms of the geometric averages of the observed and GEOS-5-calculated κ_ρ (units in m^2 s^{-1}) are shown. Also shown are (panel b) κ_ρ profiles from the free-running GEOS-5 simulation averaged over $40 - 50^o$N in the North Atlantic Ocean and averaged over all January months (lighter colors), ..., and all December months (darker colors).
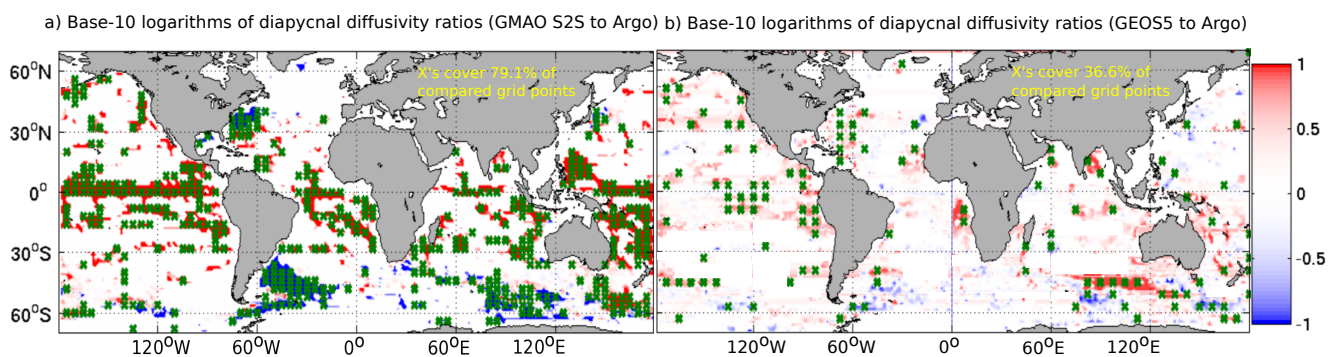
Figure A2. Shown are (a) the base-10 logarithms of the ratios of the time-averaged $\kappa_{\rho,GMAO}$ to $\kappa_{\rho,W15}$, and (b) the base-10 logarithms of the ratios of the time-averaged $\kappa_{\rho,GEOS5}$ to $\kappa_{\rho,W15}$. Each panels shows an average over 250-2000 meters depth. White areas in the ocean indicate insufficient Argo data to derive $\kappa_{\rho,W15}$. The green X's indicate regions where the disagreement between $\kappa_{\rho,GMAO}$ or $\kappa_{\rho,GEOS5}$ and $\kappa_{\rho,W15}$ is greater than a factor of 3.
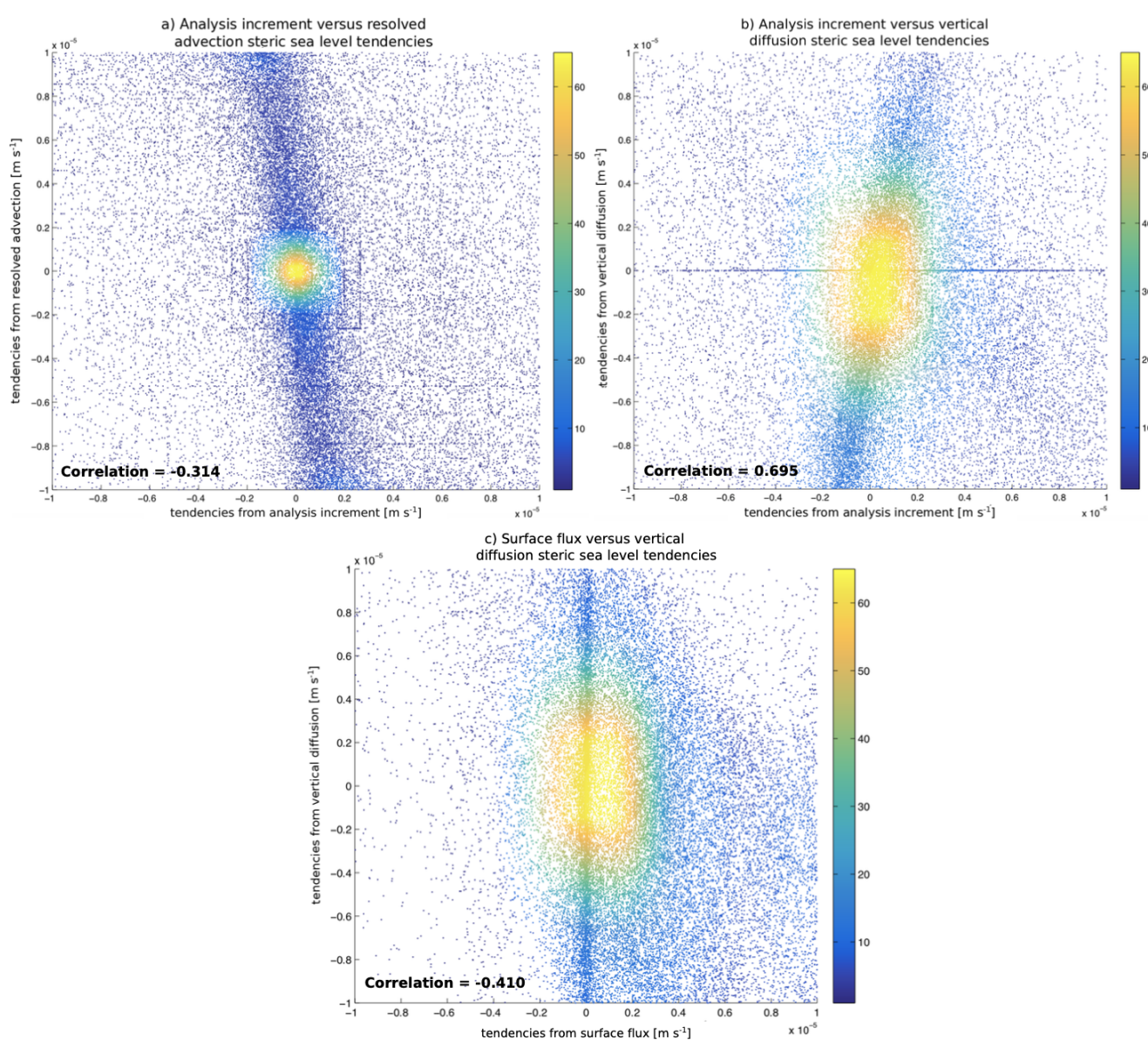
Figure A3. Scatterplots between several of the most locally dominant tendency terms in the steric sea level budget of the GMAO S2S Ocean Analysis, averaged over the entire run's time period (2012-2017): shown are (panel a) the analysis increment (abscissa) versus the resolved advection (ordinate) terms, (panel b) the analysis increment (abscissa) versus the vertical diffusion (ordinate) terms, and (panel c) the surface flux (abscissa) versus the vertical diffusion (ordinate) terms. The more yellow colors indicate a greater density of dots in the scatterplots. The more blue colors indicate a lower density of dots in the scatterplots. Also listed in each panel are the correlations between each of the comparisons.
Data availability. The data used in this study will be available through zenodo upon publication, but in the meantime, they are available at:
625 https://www.dropbox.com/s/z4w7ihzdg3hpebr/ECCOoxygenkappa.tar.gz?dl=0 . Also, the GMAO S2S Ocean Analysis output is available at:
ftp://gmaoftp.gsfc.nasa.gov/pub/data/kovach/S2S_OceanAnalysis/ . The hydrography-derived diapycnal diffusivities from the finescale pa-
rameterization used in this study, courtesy of Eric Kunze, are available by logging in as a guest at: ftp://ftp.nwra.com/outgoing/kunze/iwturb/
. The microstructure data used in this study are available at: https://microstructure.ucsd.edu/ .

Author contributions. David S. Trossman conceived of the idea, did the ECCO and GEOS-5 simulations, performed the analyses, and wrote
630 up the manuscript. Caitlin Whalen provided the Argo-derived data and helped with their use and the writing. Thomas Haine helped with the
interpretation of the results and the writing. Amy Waterhouse provided the microstructure data and helped with their use and the writing. An
Nguyen helped with the interpretation of the ECCO results and the writing. Arash Bigdeli provided help with getting the adjoint to work
with ECCO. Patrick Heimbach provided help with getting the forward MITgcm runs to get set up correctly on the TACC machines. Matthew
Mazloff helped with the interpretation of the results and the writing.

635 *Competing interests.* The authors declare no conflict of interests.

Acknowledgements. The authors thank the reviewers of this manuscript for their suggestions. David Trossman was supported by the Goddard
Earth Sciences Technology And Research (GESTAR) cooperative agreement between the GMAO of the NASA Goddard Space Flight Center
base and Johns Hopkins University as well as NASA SLCT grant 80NSSC17K0675 at the University of Texas-Austin. Thomas W. N. Haine
was supported by NOAA award NA15OAR4310172 and NSF award OCE-1338814. Amy Waterhouse was supported by NSF award OCE-
640 0968721. Caitlin Whalen was supported by National Science Foundation Award OCE-1923558. Patrick Heimbach was supported by the
ECCO project through a JPL/Caltech subcontract. An Nguyen and Arash Bigdeli were supported by NSF awards NSF-OPP-1603903 and
NSF-OPP-1708289.

The authors acknowledge the Texas Advanced Computing Center (TACC) at The University of Texas at Austin for providing HPC
resources for the ECCO simulations (URL: http://www.tacc.utexas.edu) and the NASA Center for Climate Simulation (NCCS) for the
645 computer time spent on the GEOS-5 simulations that have contributed to the research results reported within this paper.

References

Abernathey, R. P., & Marshall, J. (2013). Global surface eddy diffusivities derived from satellite altimetry. Journal of Geophysical Research: Oceans, 118, 901–916. https://doi.org/10.1002/jgrc.20066

Adcroft, A., & Campin, J.-M. (2004). Rescaled height coordinates for accurate representation of free-surface flows in ocean circulation
650 models. Ocean Modelling, 7, 269–284.

Adcroft, A., Hill, C., & Marshall, J. (1997). The representation of topography by shaved cells in a height coordinate model. Mon. Wea. Rev., 125, 2293–2315.

Alford, M.H., MacKinnon, J.A., Simmons, H.L., Nash, J.D., 2016. Near-inertial internal gravity waves in the ocean. Annual Review of Marine Science 8, 95–123.

655 Arbic, B.K., Garner, S.T., Hallberg, R.W., Simmons, H.L., 2004. The accuracy of surface elevations in forward global barotropic and baroclinic tide models. Deep Sea Research, Part II 51, 3069–3101. http://dx.doi.org/10.1016/j.dsr2.2004.09.014.

Atamanchuk, D., Koelling, J., Send, U., & Wallace, D. W. R. (2020). Rapid transfer of oxygen to the deep ocean mediated by bubbles. Nature Geoscience, 13, 232– 237. https://doi.org/10.1038/s41561-020-0532-2

Bachman, S. D., Fox-Kemper, B., & Bryan, F. O. (2020). A diagnosis of anisotropic eddy diffusion from a high-resolution global ocean
660 model. JAMES, 12, e2019MS001904. https://doi.org/10.1029/2019MS001904

Bates, M., Tulloch, R., Marshall, J., & Ferrari, R. (2014). Rationalizing the spatial distribution of mesoscale eddy diffusivity in terms of mixing length theory. Journal of Physical Oceanography, 44(6), 1523–1540. https://doi.org/10.1175/jpo-d-13-0130.1

Bigdeli, B., A. Loose, Nguyen, A. T., & Cole, S. T. (2017). Numerical investigation of the arctic ice–ocean boundary layer and implications for air–sea gas fluxes. Ocean Science, 13, 61–75. https://doi.org/10.5194/os-13-61-2017

665 Billheimer, S. J., Talley, L. D., & Martz, T. R. (2021). Oxygen seasonality, utilization rate, and impacts of vertical mixing in the eighteen degree water region of the sargasso sea as observed by profiling biogeochemical floats. Global Biogeochemical Cycles, 35, e2020GB006824. https://doi.org/10.1029/ 2020GB006824

Borovikov, A., Cullather, R., Kovach, R., Marshak, J., Vernieres, G., Vikhliaev, Y., Zhao, B., Li, Z., 2017. GEOS-5 seasonal forecast system. Climate Dynamics , 1–27, https://doi.org/10.1007/s00382-017-3835-2.

670 Brandt, P., Hahn, J., Schmidtko, S., Tuchen, F. P., Kopte, R., Kiko, R., . . .Dengler, M. (2021). Atlantic equatorial undercurrent intensification counteracts warming-induced deoxygenation. Nature Geoscience. https://doi.org/10.1038/s41561-021-00716-1

Busecke, J. J. M., & Abernathey, R. P. (2019). Ocean mesoscale mixing linked to climate variability. Science Advances, 5. https://doi.org/10.1126/sciadv.aav5014

Campin, J.-M., Adcroft, A., Hill, C., & Marshall, J. (2004). Conservation of properties in a free surface model. Ocean Modelling, 6, 221–244.

675 Chaudhuri, A. H., Ponte, R. M., Forget, G., & Heimbach, P. (2013). A comparison of atmospheric reanalysis surface products over the ocean and implications for uncertainties in air-sea boundary forcing. Journal of Climate, 26, 153–170.

Chin, M., Ginoux, P., Kinne, S., Holben, B. N. Duncan, B.N., Martin, R.V., Logan, J.A., Higurashi, A., Nakajima, T., 2002. Tropospheric aerosol optical thickness from the GOCART model and comparisons with satellite and sunphotometer measurements. Journal of Atmospheric Sciences 59, 461–483.

680 Cole, S. T., Wortham, C., Kunze, E., & Owens, W. B. (2015). Eddy stirring and horizontal diffusivity from argo float observations: Geographic and depth variability. Geophysical Research Letters, 42, 3989–3997. https://doi.org/10.1002/2015GL063827

Couespel, D., L´evy, M., & Bopp, L. (2019). Major contribution of reduced upper ocean oxygen mixing to global ocean deoxygenation in an earth system model. Geophysical Research Letters, 46, 12239–12249. https://doi.org/10.1029/2019GL084162

Dalan, F., Stone, P. H., & Sokolov, A. P. (2005). Sensitivity of the ocean's climate to diapycnal diffusivity in an EMIC. Part II: Global warming scenario. Journal of Climate, 18, 2482–2496.

Danabasoglu, G., & McWilliams, J. C. (1995). Sensitivity of the global ocean circulation to parameterizations of mesoscale tracer transports. J. Clim., 8, 2967– 2987.

D'Asaro, E. (2014). Turbulence in the upper-ocean mixed layer. Annual Review of Marine Science, 6, 101–115. https://doi.org/10.1146/annurev-marine -010213-135138

Dee, D. P., Uppala, S. M., Simmons, A. J., Berrisford, P., Poli, P., Kobayashi, S., . . . Vitart, F. (2011). The ERA-Interim reanalysis: configuration and performance of the data assimilation system. Q. J. Royal Met. Soc., 137, 553–597.

DeVries, T., & Holzer, M. (2019). Radiocarbon and helium isotope constraints on deep ocean ventilation and mantle-3he sources. Journal of Geophysical Research-Oceans, 124, 3036–3057. https://doi.org/10.1029/ 2018JC014716

Dutkiewicz, S., Sokolov, A., Scott, J., & Stone, P. (2005). A three-dimensional ocean-sea ice-carbon cycle model and its coupling to a two-dimensional atmospheric model: Uses in climate change studies. Tech. rep., MIT Joint Program of the Science and Policy of Global Change, 122. http://web.mit.edu/globalchange/www/MITJPSPGC Rpt122.pdf

Ehlert, D., Zickfeld, K., Eby, M., & Gillett, N. (2017). The sensitivity of the proportionality between temperature change and cumulative CO2 emissions to ocean mixing. Journal of Climate, 30, 2921–2935.

Ferrari, R., Griffies, S.M., Nurser, A.J.G., Vallis, G.K., 2010. A boundary-value problem for the parameterized mesoscale eddy transport. Ocean Modelling 32, 143–156.

Ferrari, R., McWilliams, J.C., Canuto, V.M., Dubovikov, M., 2008. Parameterization of eddy fluxes near oceanic boundaries. Journal of Climate 21, 2770–2789.

Forget, G., Campin, J. M., Heimbach, P., Hill, C. N., Ponte, R. M., & Wunsch, C. (2015). ECCO version 4: an integrated framework for non-linear inverse modeling and global ocean state estimation. Geosci. Model Dev., 8, 3071-3104. https://doi.org/10.5194/gmd-8-3071-2015

Forget, G., Ferreira, D., & Liang, X. (2015). On the observability of turbulent transport rates by argo: supporting evidence from an inversion experiment. Ocean Science, 11, 839–853. http://doi.org/10.5194/os-11-839-2015

Fox-Kemper, B. G. Danabasoglu, R. Ferrari, S. M. Griffies, R. W. Hallberg, M. M. Holland, M. E. Maltrud, S. Peacock, B. L. Samuels, 2011: Parameterization of mixed layer eddies. III: Implementation and impact in global ocean climate simulations. Ocean Modelling, 39, 61–78.

Fukumori, I., Wang, O., Fenty, I., Forget, G., Heimbach, P., & Ponte, R. M. (2017). Ecco version 4 release 3. DSpace MIT. http://hdl.handle.net/1721.1/ 110380

Galbraith, E. D., Dunne, J. P., Gnanadesikan, A., Slater, R. D., Sarmiento, J. L., Dufour, C. O., . . . Marvasti, S. S. (2015). Complex functionality with minimal computation: Promise and pitfalls of reduced-tracer ocean biogeochemistry models. Journal of Advances in Modeling Earth Systems, 7, 2012–2028. https://doi.org/10.1002/2015MS000463

Gaspar, P., Gr´egoris, Y., & LeFevre, J.-M. (1990). A simple eddy kinetic energy model for simulations of the oceanic vertical mixing: tests at station papa and long-term upper ocean study site. Journal of Geophysical Research, 95, 16,179–16,193.

Gelaro, R., McCarty, W., Sua´rez, M.J., Todling, R., Molod, A., Takacs, L., Randles, C.A., Darmenov, A., Bosilovich, M.G., Reichle, R., Wargan, K., Coy, L., Cullather, R., Draper, C., Akella, S., Buchard, V., Conaty, A., da Silva, A.M., Gu, W., Kim, G.K., Koster, R., Lucchesi, R., Merkova, D., Nielsen, J.E., Partyka, G., Pawson, S., Putman, W., Rienecker, M., Schubert, S.D., Sienkiewicz, M., Zhao,

B., 2017. The modern-era retrospective analysis for research and applications, version 2 (merra-2). Journal of Climate 30, 5419–5454. https://dx.doi.org10.1175/JCLI-D-16-0758.1.

Gent, P. R., & McWilliams, J. C. (1990). Isopycnal mixing in ocean circulation models. Journal of Physical Oceanography , 20 (1), 150–155. https://doi .org/10.1175/1520-0485(1990)020⟨0150:IMIOCM⟩2.0.CO;2

Gerdes, R., Ko¨berle, C., Willebrand, J., 1990. The influence of numerical advection schemes on the results of ocean general circulation models. Climate Dynamics 5, 211–226.

Giering, R., & Kaminski, T. (1998). Recipes for adjoint code construction. ACM Transactions on Mathematical Software, 24, 437–474.

Gilbert, J. C., & Lemarechal, C. (1989). Some numerical experiments with variable-storage quasi-newton algorithms. Math. Program., 45, 407–435.

Gnanadesikan, A. (1999). A simple predictive model for the structure of the oceanic pycnocline. Science, 283, 2077.

Gnanadesikan, A., Pradal, M.-A., & Abernathey, R. (2015). Isopycnal mixing by mesoscale eddies significantly impacts oceanic anthropogenic carbon uptake. Geophysical Research Letters, 42, 4249–4255. https://doi.org/10.1002/ 2015GL064100

Gregg, M. C. (1987). Diapycnal mixing in the thermocline: A review. J. Geophys. Res., 92, 5249–5286. https://doi.org/10.1029/JC092iC05p05249

Gregg, M. C. (1989). Scaling turbulent dissipation in the thermocline. Journal of Geophysical Research, 94, 9686–9698.

Gregg, M. C., D'Asaro, E. A., Riley, J. J., & Kunze, E. (2018). Mixing efficiency in the ocean. Annual Review of Marine Science, 10, 443–473.

Griewank, A. (1992). Achieving logarithmic growth of temporal and spatial complexity in reverse automatic differentiation. Optimization Methods and Software, 1, 35–54. https://doi.org/10.1080/10556789208805505

Griffies, S.M., Winton, M., Anderson, W.G., Benson, R., Delworth, T.L., Dufour, C.O., Dunne, J.P., Goddard, P., Morrison, A.K., Rosati, A., Wittenberg, A.T., Yin, J., Zhang, R., 2015. Impacts on ocean heat from transient mesoscale eddies in a hierarchy of climate models. Journal of Climate 28, 952–977.

Groeskamp, S., LaCasce, J. H., McDougall, T. J., & Rog ´e, M. (2020). Full-depth global estimates of ocean mesoscale eddy mixing from observations and theory. Geophysical Research Letters, 47, e2020GL089425. https://doi.org/10.1029/2020GL089425

Groeskamp, S., Sloyan, B. M., Zika, J. D., & McDougall, T. J. (2017). Mixing inferred from an ocean climatology and surface fluxes. Journal of Physical Oceanography, 47(3), 667–687. https://doi.org/10.1175/jpo-d-16-0125.1

Heimbach, P., Fukumori, I., Hill, C. N., Ponte, R. M., Stammer, D., Wunsch, C., . . . Zhang, H. (2019). Putting it all together: Adding value to the global ocean and climate observing systems with complete self-consistent ocean state and parameter estimates. Frontiers in Marine Science, 6. https://doi.org/10.3389/fmars.2019.00055

Heimbach, P., Menemenlis, D., Losch, M., Campin, J.-M., & Hill, C. (2010). On the formulation of sea-ice models. part 2: Lessons from multi-year adjoint sea ice export sensitivities through the canadian arctic archipelago. Ocean Modelling, 33, 145–158. https://doi.org/10.1016/j.ocemod.2010.02.002

Henyey, F. S., Wright, J., & Flatt ´e, S. M. (1986). Energy and action flow through the internal wave field: an Eikonal approach. Journal of Geophysical Research, 91, 8487–8495.

Hieronymus, M., Nycander, J., Nilsson, J., D ¨o ¨os, K., & Hallberg, R. (2019). Oceanic overturning and heat transport: the role of background diffusivity. Journal of Climate, 32, 701–716.

Holmes, R. M., Zika, J. D., Griffies, S. M., McC Hogg, A., Kiss, A. E., & England, M. H. (2021). The geography of numerical mixing in a suite of global ocean models. Journal of Advances in Modeling Earth Systems, 13. https://doi.org/10.1029/2020MS002333

Hunke, E.C., Lipscomb, W.H., Turner, A.K., Jeffery, N., Elliott, S., 2013. Cice: the los alamos sea ice model documentation and software user's manual version 5.0. Los Alamos National Laboratory LA-CC-06-012.

Katsumata, K. (2016). Eddies observed by Argo floats. part I: Eddy transport in the upper 1000 dbar. Journal of Physical Oceanography, 46, 3471–3486. https://doi.org/10.1175/JPO-D-16-0150.1

Khatiwala, S., Primeau, F., & Hall, T. M. (2009). Reconstruction of the history of anthropogenic co2 concentrations in the ocean. Nature, 462, 346–349. https://doi.org/10.1038/nature08526

Krasting, J., Stouffer, R., Griffies, S., Hallberg, R., Malyshev, S., Samuels, B., & Sentman, L. (2018). Role of ocean model formulation in climate response uncertainty. Journal of Climate, 31, 9313–9332.

Kunze, E. (2017). Internal-wave-driven mixing: Global geography and budgets. Journal of Physical Oceanography, 47, 1325–1345.

Large, W. G., McWilliams, J. C., & Doney, S. C. (1994). Oceanic vertical mixing: a review and a model with a nonlocal boundary layer parameterization. Reviews of Geophysics, 32, 363–403.

Large, W. G., & Yeager, S. G. (2009). The global climatology of an interannually varying air-sea flux data set. Climate Dynamics, 33, 341–364.

Ledwell, J. R., & Watson, A. J. (1991). The Santa Monica basin tracer experiment: A study of diapycnal and isopycnal mixing. Journal of Geophysical Research, 96, 8695–8718. https://doi.org/10.1029/91JC00102

Liu, C., Kohl, A., & Stammer, D. (2012). Adjoint-based estimation of eddy-induced tracer mixing parameters in the global ocean. J. Phys. Oceanogr., 42, 1186– 1206.

Loose, N., & Heimbach, P. (2021). Leveraging uncertainty quantification to design ocean climate observing systems. Journal of Advances in Modeling Earth Systems, 13. https://doi.org/10.1029/2020MS002386

Losch, M., Menemenlis, D., Campin, J.-M., Heimbach, P., & Hill, C. (2010). On the formulation of sea-ice models. part 1: Effects of different solver implementations and parameterizations. Ocean Modelling, 33, 129–144. https://doi.org/10.1016/j.ocemod.2009.12.008

Lueck, R. G., Huang, D., Newman, D., & Box, J. (1997). Turbulence measurement with a moored instrument. Journal of Atmospheric and Oceanic Technology, 14, 143–161. https://doi.org/10.1175/1520-0426(1997)014⟨0143: TMWAMI⟩2.0.CO;2

MacKinnon, J., Zhao, Z., Whalen, C. B., Waterhouse, A. F., Trossman, D. S., Sun, O. M., . . . Alford, M. H. (2017). Climate process team on internal-wave driven ocean mixing. Bulletin of the American Meteorological Society, 98, 2429–2454. http://dx.doi.org/10.1175/BAMS-D-16-0030.1

Manikandan, S. (2011). Measures of central tendency: The mean. Journal of Phamacol Pharmacother, 2, 140–142.

Markus, T., Cavalieri, D.J., 2009. The AMSR-E NT2 sea ice concentration algorithm: its basis and implementation. Journal of The Remote Sensing Society of Japan 29, 216–225. https://doi.org/10.11440/rssj.29.216.

Masuda, S., & Osafune, S. (2021). Ocean state estimations for synthesis of ocean-mixing observations. Journal of Oceanography. https://doi.org/10.1007/ s10872-020-00587-x

Melet, A., Hallberg, R., Legg, S., Nikurashin, M., 2014. Sensitivity of the ocean state to lee wave-driven mixing. Journal of Physical Oceanography, 44, 900–921.

Melet, A., Legg, S., Hallberg, R., 2016. Climatic impacts of parameterized local and remote tidal mixing. Journal of Climate 29, 3473–3500. http://dx.doi.org/10.1175/JCLI-D-15-0153.1.

Melet, A., Nikurashin, M., Muller, C., Falahat, S., Nycander, J., Timko, P.G., Arbic, B.K., Goff, J.A., 2013. Internal tide generation by abyssal hills using analytical theory. Journal of Geophysical Research-Oceans 118, 6303–6318.

Menemenlis, D., Fukumori, I., & Lee, T. (2005). Using Green's functions to calibrate and ocean general circulation model. Monthly Weather Review, 133(5), 1224–1240. https://doi.org/10.1175/MWR2912.1

Mesinger, F., Arakawa, A., 1976. Numerical methods used in atmospheric models, in: WMO/ICSU Joint Organizing Committee. GARP Publ. Series, p. 64.

Messias, M.-J., Watson, A. J., Johannessen, T., Oliver, K. I. C., Olsson, K. A., Fogelqvist, E., . . . Ledwell, J. R. (2008). The Greenland sea tracer experiment 1996-2002: Horizontal mixing and transport of Greenland sea intermediate water. Progress in Oceanography, 78, 85–105. https://doi.org/10.1016/ j.pocean.2007.06.005

Molod, A., Hackert, E., Vikhliaev, Y., Zhao, B., Barahona, D., Vernieres, G., et al., 2020. Geos-s2s version 2: The gmao high-resolution coupled model and assimilation system for seasonal prediction. Journal of Geophysical Research: Atmospheres 125, e2019JD031767. https://doi.org/10.1029/2019JD031767.

Molod, A., Takacs, L., Suarez, M., Bacmeister, J., 2015. Development of the geos-5 atmospheric general circulation model: evolution from merra to merra-2. Geoscientific Model Development 8, 1339–1356. https://doi.org/10.5194/gmd-8-1339-2015.

Molod, A., Takacs, L., Suarez, M., Bacmeister, J., Song, I.S., Eichmann, A., 2012. The geos-5 atmospheric general circulation model: Mean climate and development from merra to fortuna. Technical Report Series on Global Modeling and Data Assimilation 28.

Moum, J. N., Caldwell, D. R., Nash, J. D., & Gunderson, G. D. (2002). Observations of boundary mixing over the continental slope. Journal of Physical Oceanography, 32, 2113–2130. https://doi.org/10.1175/1520-0485(2002)032⟨2113:OOBMOT⟩2.0.CO;2

Munk, W., & Wunsch, C. (1998). Abyssal recipes II: Energetics of tidal and wind mixing. Deep Sea Research, Part I, 45, 1977–2010.

Murray, R.J., 1996. Explicit generation of orthogonal grids for ocean models. Journal of Computational Physics 126, 251–273.

Naveira Garabato, A.C., Nurser, A.G., Scott, R.B., Goff, J.A., 2013. The impact of small-scale topography on the dynamical balance of the ocean. Journal of Physical Oceanography 43, 647–668.

Nikurashin, M., Ferrari, R., 2011. Global energy conversion rate from geostrophic flows into internal lee waves in the deep ocean. Geophysical Research Letters 38, L08610. http://doi.org/10.1029/2011GL046576.

Nocedal, J. (1980). Updating quasi-newton matrices with limited storage. Mathematics of Computation, 35, 773–782.

Nycander, J., 2005. Generation of internal waves in the deep ocean by tides. Journal of Geophysical Research 110, C10028. http://doi.org/10.1029/2004JC002487.

Osborn, T. R. (1980). Estimates of the local rate of vertical diffusion from dissipation measurements. Journal of Physical Oceanography, 10, 83–89.

Palter, J.B., Griffies, S.M., Galbraith, E.D., Gnanadesikan, A., Samuels, B., Klocker, A., 2014. The driving processes of the deep ocean buoyancy budget and their temporal variability. Journal of Climate 27, 551–573.

Palter, J. B., & Trossman, D. S. (2018). The sensitivity of future ocean oxygen to changes in ocean circulation. Global Biogeochemical Cycles, 32, 738–751. https://doi.org/10.1002/2017GB005777

Penny, S.G., Kalnay, E., Carton, J.A., Hunt, B.R., Ide, K., Miyoshi, T., Chepurin, G.A., 2013. The local ensemble transform kalman filter and the running-in-place algorithm applied to a global ocean general circulation model. Nonlinear Processes in Geophysics 20, 1031–1046. http: //doi.org/10.5194/npg-20-1031-2013.

Pilo, G.S., Oke, P.R., Coleman, R., Rykova, T., Ridgway, K., 2018. Impact of data assimilation on vertical velocities in an eddy resolving ocean model. Ocean Modelling 131, 71–85.

Polzin, K. L., Naveira Garabato, A. C., Huussen, T. N., Sloyan, B. N., & Waterman, S. (2014). Finescale parameterizations of turbulent dissipation. Journal of Geophysical Research-Oceans, 119, 1383–1419. https://doi.org/10.1002/2013JC008979

Polzin, K. L., Toole, J. M., Ledwell, J. R., & Schmitt, R. W. (1997). Spatial variability of turbulent mixing in the abyssal ocean. Science, 276, 93–96. https://doi.org/10.1126/science.276.5309.93

Polzin, K. L., Toole, J. M., & Schmitt, R. W. (1995). Finescale parameterizations of turbulent dissipation. Journal of Physical Oceanography, 25, 306–328.

Redi, M. H. (1982). Oceanic isopycnal mixing by coordinate rotation. J. Phys. Oceanogr., 12, 1154–1158.

Reichle, R., Koster, R., De Lannoy, G., Forman, B., Liu, Q., Mahanama, S., Touré, A., 2011. Assessment and enhancement of merra land surface hydrology estimates. Journal of Climate 24, 6322–6338. https://doi.org/10.1175/JCLI-D-10-05033.1.

Roach, C. J., Balwada, D., & Speer, K. (2018). Global observations of horizontal mixing from Argo float and surface drifter trajectories. Journal of Geophysical Research: Oceans, 123. https://doi.org/10.1029/2018JC013750

Scott, J. R., & Marotzke, J. (2002). The location of diapycnal mixing and the meridional overturning circulation. Journal of Physical Oceanography, 32, 3578–3595.

Scott, R.B., Goff, J.A., Naveira-Garabato, A.C., Nurser, A.J.G., 2011. Global rate and spectral characteristics of internal gravity wave generation by geostrophic flow over topography. Journal of Geophysical Research-Oceans 116, C09029. https://doi.org/10.1029/2011JC007005.

Simmons, H.L., Jayne, S.R., St. Laurent, L.C., Weaver, A.J., 2004. Tidally driven mixing in a numerical model of the general circulation. Ocean Modelling 6, 245–263.

Sinha, B., Sévellec, F., Robson, J., & Nurser, G. (2020). Surging of global surface temperature due to decadal legacy of ocean heat uptake. Journal of Climate. https://doi.org/10.1175/JCLI-D-19-0874.1

Stammer, D., Balmaseda, M., Heimbach, P., Köhl, A., & Weaver, A. (2016). Ocean data assimilation in support of climate applications: status and perspectives. Ann. Rev. Mar. Sci., 8, 491–518. https://doi.org/10.1146/ annurev-marine-122414-034113

Stammer, D., Wunsch, C., Giering, R., Eckert, C., Heimbach, P., Marotzke, J., . . . Marshall, J. (2002). Global ocean circulation during 1992-1997, estimated from ocean observations and a general circulation model. Journal of Geophysical Research, 107, 3118. https://doi.org/10.1029/2001JC000888

St. Laurent, L., & Schmitt, R. (1999). The contribution of salt fingers to vertical mixing in the north Atlantic tracer release experiment. Journal of Physical Oceanography, 29, 1404–1424.

Thorpe, S. (2007). In An introduction to ocean turbulence. Cambridge University Press. https://doi.org/10.1017/CBO9780511801198

Treguier, A.M., 1992. Kinetic energy analysis of an eddy resolving, primitive equation model of the North Atlantic. Journal of Geophysical Research, 97, 687–701.

Trossman, D.S., Arbic, B.K., Garner, S.T., Goff, J.A., Jayne, S.R., Metzger, E.J., Wallcraft, A.J., 2013. Impact of parameterized lee wave drag on the energy budget of an eddying global ocean model. Ocean Modelling 72, 119–142.

Trossman, D.S., Arbic, B.K., Richman, J.G., Garner, S.T., Jayne, S.R., Wallcraft, A.J., 2016. Impact of topographic internal lee wave drag on an eddying global ocean model. Ocean Modelling 97, 109–128.

Verdy, A., & Mazloff, M. R. (2017). A data assimilating model for estimating Southern Ocean biogeochemistry. Journal of Geophysical Research-Oceans, 122, 6968–6988. https://doi.org/10.1002/2016JC012650

Waterhouse, A. F., MacKinnon, J. A., Nash, J. D., Alford, M. H., Kunze, E., Simmons, H. L., . . . Lee, C. M. (2014). Global patterns of diapycnal mixing from measurements of the turbulent dissipation rate. Journal of Physical Oceanography, 44, 1854–1872.

Whalen, C., C. B. de Lavergne, Naveira Garabato, A. C., Klymak, J. M., MacKinnon, J. A., & Sheen, K. L. (2020). Internal wave-driven mixing: governing processes and consequences for climate. Nature Reviews Earth & Environment, 1, 606–621. https://doi.org/10.1038/s43017-020-0097-z

870 Whalen, C. B., MacKinnon, J. A., Talley, L. D., & Waterhouse, A. F. (2015). Estimating the mean diapycnal mixing using a finescale strain parameterization. Journal of Physical Oceanography, 45, 1174–1188.

Wright, C.J., Scott, R.B., Ailliot, P., Furnival, D., 2014. Lee wave generation rates in the deep ocean. Geophysical Research Letters 41, 2434–2440. https://doi.org/10.1002/2013GL059087.

Wunsch, C. (2006). In The ocean circulation inverse problem. Cambridge University Press. https://doi.org/10.1017/CBO9780511629570

875 Wunsch, C., & Heimbach, P. (2007, June). Practical global oceanic state estimation. Physica D: Nonlinear Phenomena, 230(1-2), 197–208. https://doi.org/10.1016/j.physd.2006.09.040

Yang, L., Nikurashin, M., Hogg, A.M., Sloyan, B.M., 2018. Energy loss from transient eddies due to lee wave generation in the Southern Ocean. Journal of Physical Oceanography 48, 2867–2885.

Zanna, L., Khatiwala, S., Gregory, J. M., Ison, J., & Heimbach, P., 2019: Global reconstruction of historical ocean heat storage and transport.

880 Proceedings of the National Academy of Sciences, 116, 1126–1131. https://doi.org/10.1073/pnas.1808838115
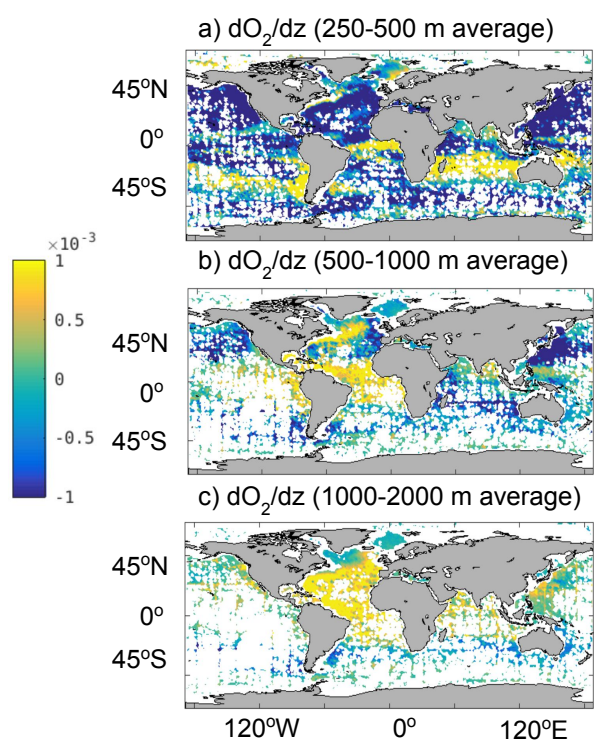
Figure 1. Shown are the vertical gradients of oxygen concentrations (units in ml/l/m) from the World Ocean Atlas (2013). Panel a shows an average over 250-500 meters depth. Panel b shows an average over 500-1000 meters depth. Panel c shows an average over 1000-2000 meters depth. White areas in the ocean indicate insufficient data.
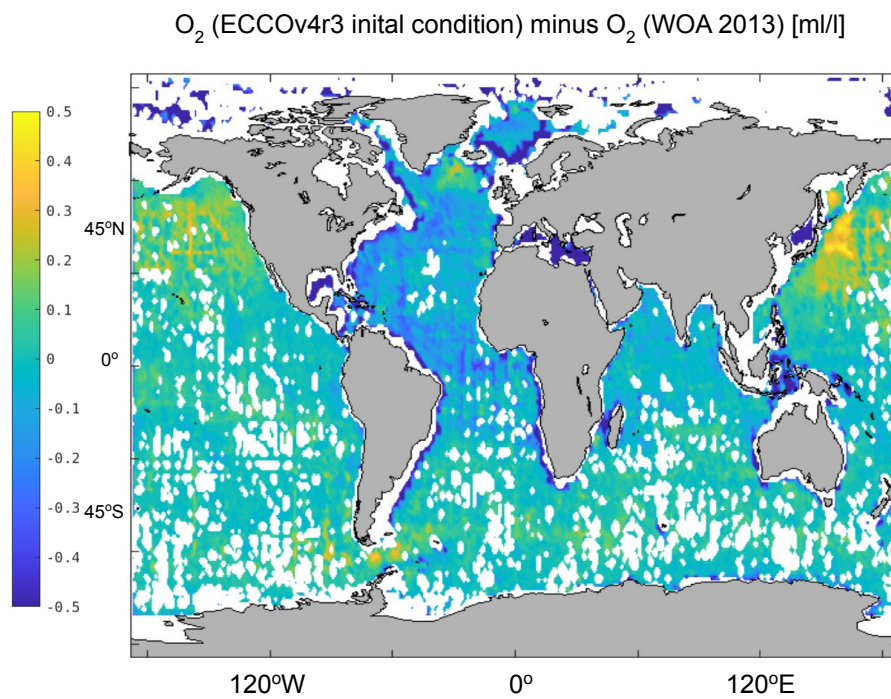
Figure 2. Shown are the average differences between the oxygen concentrations' initial conditions (units in ml/l) used for the ECCO adjoint sensitivity experiments and the observational climatologies from the World Ocean Atlas (2013) in the model's cost function. White areas in the ocean indicate insufficient data.
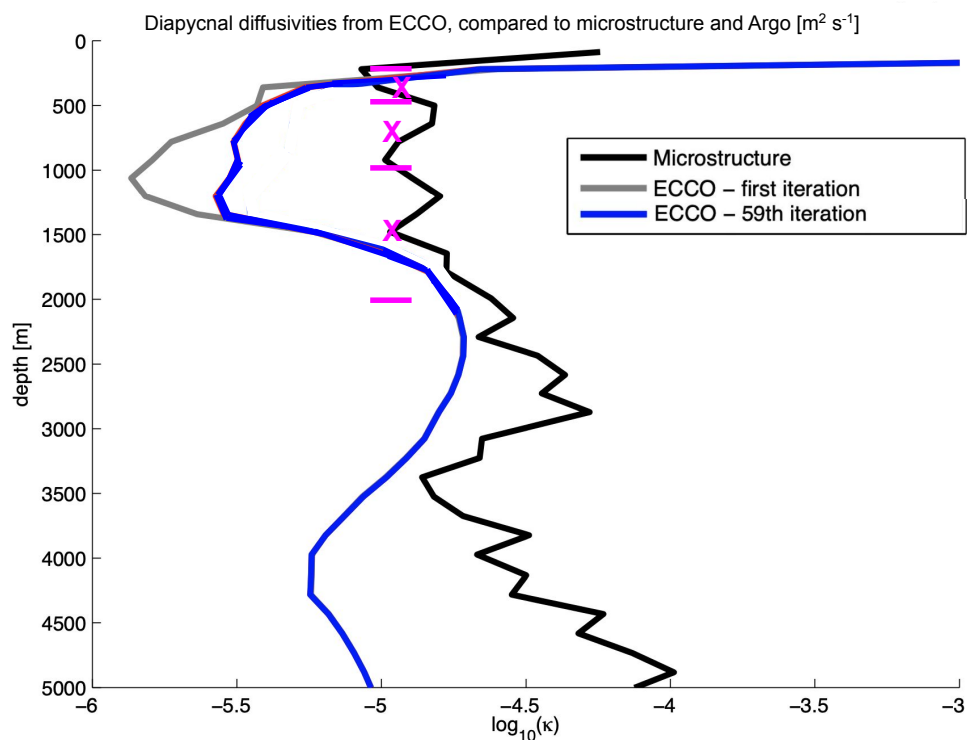
Figure 3. κ_ρ profiles averaged over all microstructure observation locations and over the length of the ECCO simulations from the first iteration of the optimization (E-CTRL$_0$ - grey curve), and from the (final) fifty-ninth iteration of the optimization (E-CTRL - red curve). Also shown is the average of κ_ρ profiles from the 24 full-depth microstructure observations (black curve) presented in *Waterhouse et al.* (2014) (see their Fig. 6; also see Figs. 4b,d,f of the present study) and the average of κ_ρ (magenta X's bounded by horizontal lines) at each of the depth bins in the *Whalen et al.* (2015) product. At each location, the simulated profiles are extracted and the base-10 logarithms of the geometric averages of the observed and ECCO-estimated κ_ρ (units in m^2 s^{-1}) are shown.
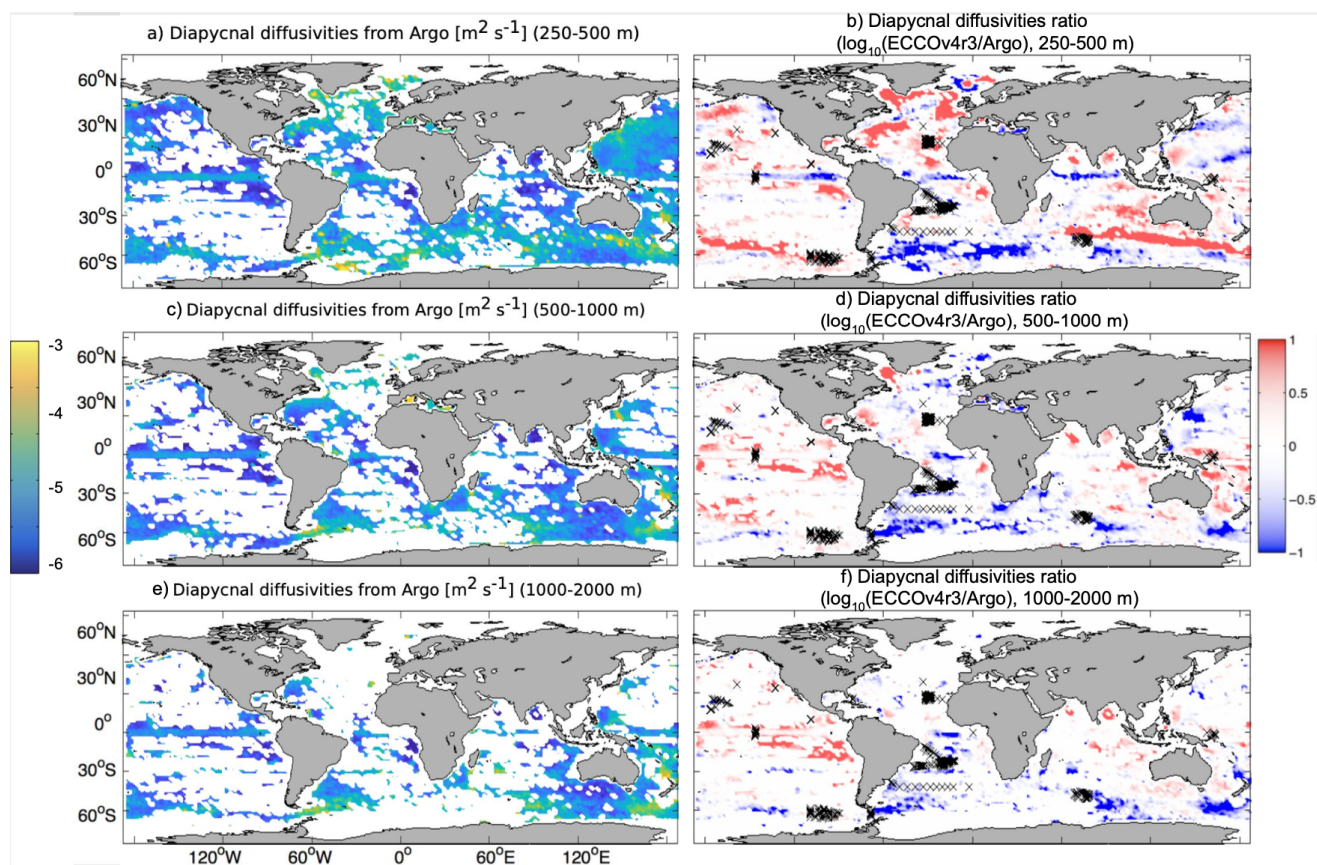
Figure 4. Shown are (a,c,e) the base-10 logarithms of $\kappa_{\rho,W15}$ (units in m^2 s^{-1}) and (b,d,f) the base-10 logarithms of the ratios of the time-averaged $\kappa_{\rho,ECCO}$ to $\kappa_{\rho,W15}$. Panels a-b show an average over 250-500 meters depth. Panels c-d show an average over 500-1000 meters depth. Panels e-f show an average over 1000-2000 meters depth. White areas in the ocean indicate insufficient Argo data to derive $\kappa_{\rho,W15}$. Black X's indicate locations where there are microstructure profiles used in Fig. 3.
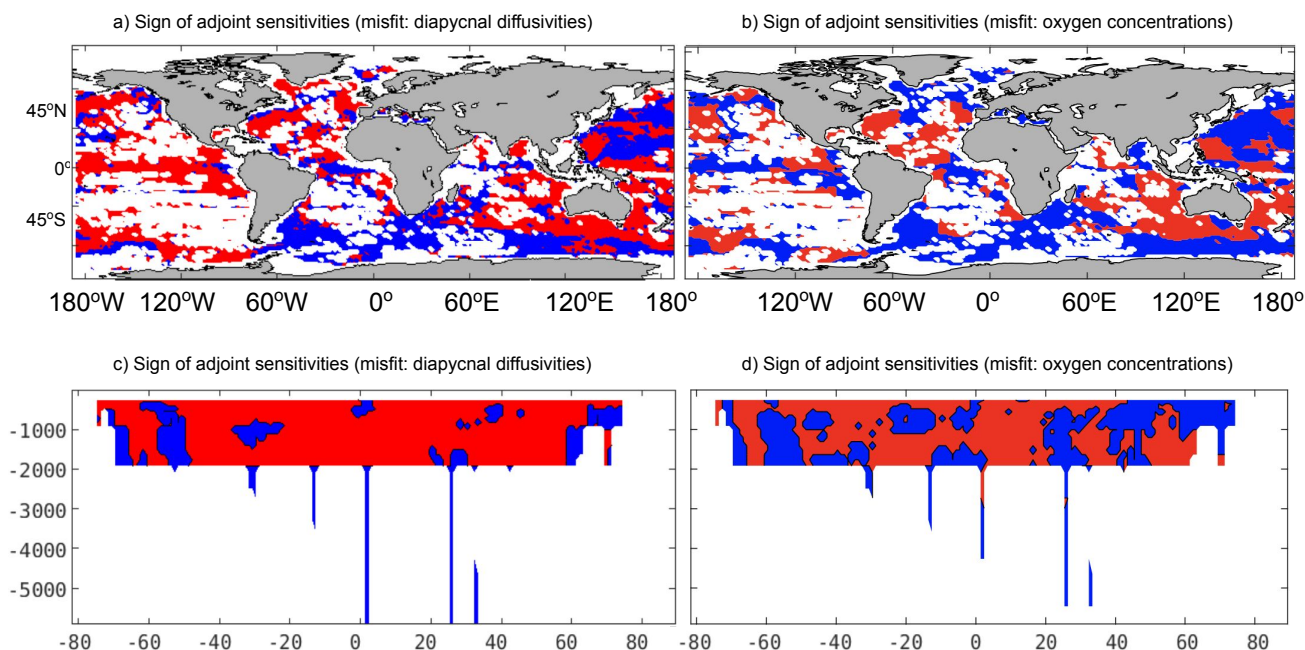
Figure 5. Adjoint sensitivity sign comparisons: Results from E_κ (panels a and c) and E_O (panels b and d) are shown for the adjoint sensitivities (units in s m^{-2}) with respect to κ_ρ: averaged over 250-2000 meters depth (panels a-b) and zonally averaged (panels c-d). The red regions indicate that the adjoint sensitivities are positive ($\partial J / \partial \kappa_\rho > 0$) and blue regions indicate negative adjoint sensitivities. $\kappa_{\rho,W15}$ and $\kappa_{\rho,K17}$ are the only quantities used in the misfit calculation of an adjoint run shown in panels a and c. The climatological oxygen concentrations from the World Ocean Atlas (2013) are the only observations used in the misfit calculation of a separate adjoint run shown in panels b and d. The adjoint sensitivities in panels a and c are computed offline (i.e., not using ECCO, but by plugging in the value the model reads in for the base-10 logarithm of κ_ρ and comparing that with the above observationally-derived base-10 logarithm of the κ_ρ products using the finescale parameterization via Eq. 2). The adjoint sensitivities in panels b and d are computed online (i.e., using ECCO, which uses the base-10 logarithm of κ_ρ as a control variable). The white regions are locations with bathymetry or insufficient observations. The adjoint sensitivities are calculated over just one year (1992).
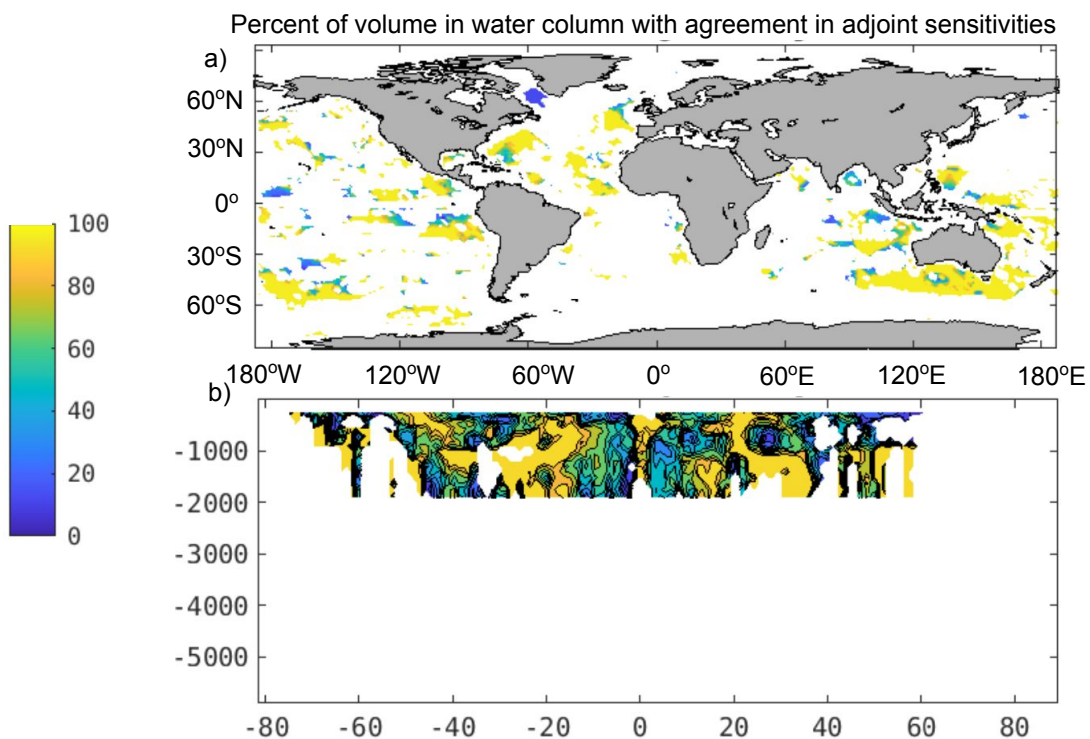
Figure 6. Shown are the percents of volume over the water column for each horizontal location (panel a) and percent of volume over all longitudes for each depth and latitude (panel b) where the sign of $\partial J/\partial \kappa_\rho$ agrees between E_κ and E_O. The white areas are locations where the disagreements between $\kappa_{\rho,ECCO}$ and $\kappa_{\rho,W15}$ supplemented with $\kappa_{\rho,K17}$ are within three times the value fo the observationally-derived κ_ρ so these were excluded.
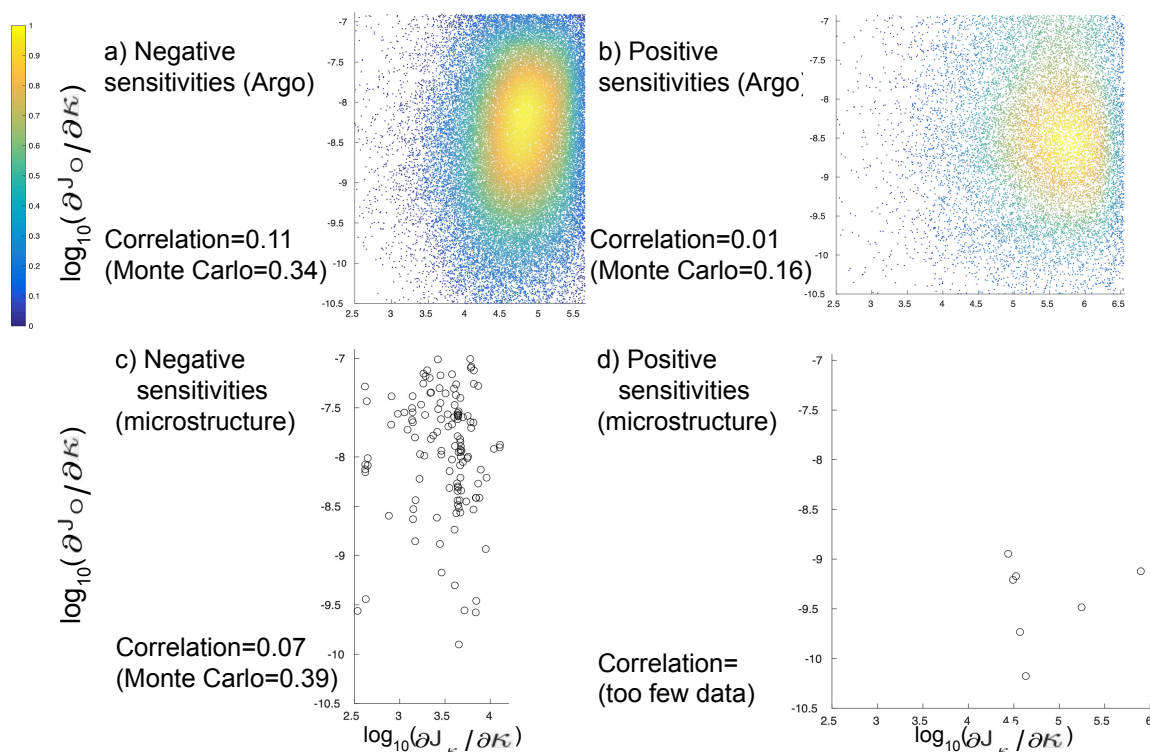
Figure 7. Shown are scatterplots between the adjoint sensitivities from E_O and E_κ where they are both negative (panels a and c) and where they are both positive (panels b and d), where E_κ has its adjoint sensitivities calculated with either Argo-derived κ_ρ ($\kappa_{\rho,W15}$ and $\kappa_{\rho,K17}$; panels a-b) or microstructure-inferred κ_ρ (panels c-d). Only the adjoint sensitivities where the differences between $\kappa_{\rho,ECCO}$ and observational κ_ρ products are statistically significant (greater than a factor of three) and where the differences between oxygen concentrations from ECCO and those from the World Ocean Atlas (2013) are statistically insignificant (within 2% of the latter) are included. The correlations for all of the data points shown in each panel are listed. Also listed below each panel are the maximum possible correlations from a Monte Carlo-based approach in which 10,000 random samples of κ_ρ within the uncertainties of the observational κ_ρ products are used to recompute the adjoint sensitivities for E_κ.

Table 1. The latitude and depth ranges of each observationally-derived product from a parameterization used in this study. The longitude range for each dataset spans $(180^o E, 180^o W)$. Also listed is the time period of the observations each product is based on and the range of values in each product (to the nearest order of magnitude in units of $\mathrm{m}^2\mathrm{s}^{-1}$).

data source	range [$\mathrm{m}^2\mathrm{s}^{-1}$]	latitude range	depth range	time period
Argo ($\kappa_{\rho,W15}$)	$(10^{-7}, 10^{-2})$	$(75^o S, 75^o N)$	(250,2000)	2006-2014
Ship-based CTD hydrography ($\kappa_{\rho,K17}$)	$(10^{-8}, 10^{-3})$	$(77.35^o S, 78.70^o N)$	(173,6044.5)	1981-2010

Table 2. Listed are the ECCO simulations performed and analyzed in the present study as well as the observationally-derived data or measured data included in each simulation. Either observationally-derived data or measured data are included in the experiments through its misfit calculation (Eq. 1). Here, κ_ρ denotes an observationally-derived κ_ρ product from the finescale parameteration, $\epsilon = \kappa_\rho N^2/0.2$ indicates an observationally-derived dissipation rate (N^2 is the stratification from the World Ocean Atlas or *WOA* (2013)), and O$_2$ is the climatology of measured oxygen concentrations from *WOA* (2013). The misfits for the experiments with κ_ρ and ϵ are calculated using Eq. 2.

experiment	observationally-derived data	measured data
E-CTRL	N/A	see Section 2.2.1
E_κ	$\kappa_{\rho,W15}, \kappa_{\rho,K17}$	N/A
E_O	N/A	O$_2$ [*WOA*, 2013]
E_ϵ	$\kappa_{\rho,W15}, \kappa_{\rho,K17}$	T/S [*WOA*, 2013]

Table 3. The cost functions of the adjoint sensitivity ECCO runs for each data sources. Listed are the globally computed values and the number of data points used.

experiment	data source	cost function	number of data points
E_κ	Argo	1.91×10^{17}	5.933×10^4
E_κ	Ship-based CTD hydrography	2.89×10^{18}	7.3806×10^4
E_O	O$_2$ WOA (2013)	7.71×10^4	7.9752×10^4

Table 4. Listed are the percent volumes where the signs of the adjoint sensitivities agree between E_κ and E_O for different regions of the ocean. The boundaries of subtropical/equatorial regions are set to be at 20^oN/S. The boundaries of subtropical/subpolar or subtropical/Southern Ocean regions are set to be 50^oN/S. The percentages are only calculated where sufficient observations are available to derive κ_ρ and where the difference between the model-calculated and observationally-derived κ_ρ is greater than the uncertainty (i.e., three times the observationally-derived κ_ρ). In parentheses are the same, except for the dissipation rates, $\epsilon_\rho = N^2\kappa_\rho/0.2$, where N^2 is the stratification and 0.2 is an empirical coefficient (see, e.g., *Gregg et al.* (2018)).

region	percent of ocean volume with agreement
Global	60.8% (59.9%)
Subtropics	72.3% (72.9%)
Subtropical South Pacific	76.9% (79.2%)
Equatorial Pacific	57.9% (54.9%)
Subtropical North Pacific	60.4% (59.6%)
Southern	49.5% (47.9%)
Indian	67.8% (68.7%)
Subtropical South Atlantic	44.6% (35.8%)
Equatorial Atlantic	62.1% (62.1%)
Subtropical North Atlantic	84.7% (85.4%)
Subpolar North Atlantic	12.7% (12.8%)